TECHNISCHE
UNIVERSITÄT
WIEN

ATOMINSTITUT

MEDIZINISCHE
UNIVERSITÄT WIEN

Dᴜᴘʟᴏᴍᴀʀʙᴇɪᴛ

Beam Model Creation and Dosimetric Validation for Preclinical Research with X-rays

zur Erlangung des akademischen Grades

Diplom-Ingenieurin

im Rahmen des Studiums

Physikalische Energie- und Messtechnik

eingereicht von

Dangl Verena
Matrikelnummer 01426510

ausgeführt am
Atominstitut der Fakultät für Physik der Technische Universität Wien

in Zusammenarbeit mit der
Universitätsklinik für Radioonkologie der Medizinische Universität Wien

Betreuung
Univ.-Prof. Dipl.-Ing. Dr.techn. Dietmar Georg
Mag. Barbara Knäusl, PhD
Mag. Peter Kuess, PhD

Wien, 17.05.2023

_____   _____
(Unterschrift Verfasserin)   (Unterschrift Betreuer)

TU Bibliothek
Your knowledge hub
WIEN

Abstract

Medical research in the field of cancer therapy is crucial, as cancer is one of the most common causes of death. Radiotherapy is one of the main pillars in cancer therapy and ongoing research aims to improve and expand treatment methods. Pre-clinical in-vivo studies are the final step in the transition from in-vitro cell experiments to clinical application. A prerequisite in small animal research is to reproduce the conditions of radiation therapy (RT) on humans as closely as possible. This indicates that scaling down the entire geometry is essential.

In collaboration with the MedAustron Ion Therapy Center (Wiener Neustadt, Austria) and the University of Applied Sciences Wiener Neustadt (Wiener Neustadt, Austria) the Department of Radiation Oncology at the Medical University of Vienna is currently working on establishing the technological basis for high precision image-guided irradiation of small animals with ion beams and kilovoltage X-rays.

In this thesis, a beam model for a 200 keV photon beam was developed, which is used as reference irradiation system. The beam model was created in the treatment planning system (TPS) µ-RayStation (RaySearch Laboratories, Stockholm, Sweden), which is specially designed to create dose maps for small animals.

In prior work, a measurement setup was developed consisting of an in-house developed beam collimation system, a positioning table and a couch for the anaesthetised small animal, as well as a small field dosimetry phantom (SFDP) for dosimetric measurements. The collimation system consists of a primary collimator (PC) and various exchangeable secondary collimators (SCs) with diameters between 5 mm and 30 mm. Crucial for the accuracy of the beam model was the characterisation of the collimated photon beam. For this purpose, depth dose profiles (DDPs) and lateral dose profiles (LDPs) of the beam were measured using the SFDP with Gafchromic$^{\text{TM}}$ EBT3 films (Ashland Inc., Wayne, NJ, USA) and a microDiamond detector (PTW-Freiburg, Germany). The field sizes of the SCs were determined with the LDPs taken at the reference point. The 8 mm aperture was chosen as reference field size and the dose rate was measured for this field size at the reference point. The evaluated measurement data was imported into the TPS and irradiation plans were prepared for the validation of the beam model. Targets for the 5 mm, 8 mm, 15 mm and 30 mm diameter SCs were created in the planning module of the TPS and positioned at different depths (3 mm, 10 mm, 30 mm, 50 mm). For these targets, treatment plans with a prescribed dose of 100, 200 and 500 cGy were created. Hence, the dose distribution and the required irradiation time for the photon beam were calculated by the TPS.

To validate the beam model, the deviations between calculated and measured dose

were determined. The dose was measured in the SFDP with the microDiamond detector. The best agreement was found for the 8 mm aperture, which was also used as reference field size of the beam model. For this 8 mm SC, in total 10 treatment plans were validated with a maximum deviation of under 2%. For the larger SCs, the dose was underestimated by the TPS by up to +8.8% for the 30 mm aperture and +5.9% for the 15 mm aperture. The largest deviations were found for the 5 mm aperture. In 50 mm water equivalent depth (WED) -10.2% dose deviation was measured.

Considering the measurement depths, the mean relative deviations were between -0.7% and +2.2%. The highest average deviation of +2.2% was found for the measurements close to the surface in 3 mm WED. The best agreement with ±0.1% mean relative deviation was found for the values in 11 mm WED and 51 mm WED. The determined deviations were in agreement with reports in recent literature about similar studies.

The dose deviations for the smallest SC (5 mm) underlined the requirements of accurate positioning. However, the currently used positioning table is limited in its stability, resulting in a decreased level of accuracy. Therefore, an improved version of the table is highly desired to enhance precision and reliability.

Kurzfassung

Die Forschung auf dem Gebiet der Krebstherapie ist für die Medizin von großer Bedeutung, da Krebs heutzutage eine der häufigsten Todesursachen ist. Die Strahlentherapie ist eine der wichtigsten Säulen der Krebstherapie, und die laufende Forschung zielt darauf ab, die Behandlungsmethoden zu verbessern und zu erweitern.

Präklinische in-vivo Studien sind der letzte Schritt von in-vitro Zellexperimenten zur klinischen Anwendung. Ziel ist es, die Bedingungen der Strahlentherapie am Menschen so ähnlich wie möglich für die Kleintierforschung nachzubilden. Das bedeutet, dass das gesamte System auf diese Maßstäbe verkleinert werden muss. In Zusammenarbeit mit dem Ionentherapiezentrum MedAustron (Wiener Neustadt, Österreich) und der Fachhochschule Wiener Neustadt (Wiener Neustadt, Österreich) arbeitet die Abteilung für Radioonkologie der Medizinischen Universität Wien derzeit daran, die technologischen Grundlagen für die bildgesteuerte Bestrahlung von Kleintieren mit Ionen- und Röntgenstrahlen zu schaffen.

In dieser Diplomarbeit wurde ein Beam-Modell für einen 200 keV Photonenstrahl entwickelt, der für Referenzbestrahlungen verwendet wird. Das Beam-Modell wurde in dem Bestrahlungsplanungssystem μ-RayStation (RaySearch Laboratories, Stockholm, Sweden) erstellt, das für die Erstellung von Dosisverteilungen im Bereich der Kleintierbestrahlung angepasst ist.

In vorausgehenden Projekten wurde bereits ein Messaufbau entwickelt, der aus einem Kollimatorsystem, einem beweglichen Tisch und einem Maus-Bett zur Positionierung des betäubten Kleintiers und einem Kleinfeld-Dosimetrie-Phantom für Dosismessungen besteht. Das Kollimatorsystem besteht aus einem Primärkollimator und austauschbaren Sekundärkollimatoren mit Feldgrößendurchmessern zwischen 5 mm und 30 mm. Entscheidend für die Genauigkeit des Strahlmodells war die Charakterisierung des kollimierten Photonenstrahls. Hierfür wurden Tiefendosisprofile und laterale Dosisprofile im Phantom mit Gafchromic™ EBT3 Filmen (Ashland Inc., Wayne, NJ, USA) und einem microDiamond Detektor (PTW-Freiburg, Germany) gemessen. Die Feldgrößen der Sekundärkollimatoren wurden mittels der lateralen Dosisprofile im Referenzpunkt bestimmt. Der Sekundärkollimator mit 8 mm Durchmesser wurde als Kollimator für das Referenzfeld gewählt und die Dosisleistung für diese Feldgröße im Referenzpunkt gemessen. Die ausgewerteten Messdaten wurden in das Planungssystem importiert und Bestrahlungspläne zur Validierung des Beam-Modells erstellt. Für die Kollimator mit 5 mm, 8 mm, 15 mm und 30 mm Durchmesser wurden im Planungsmodul des TPS Targets erstellt und in verschiedenen Tiefen (3 mm, 10 mm, 30 mm, 50 mm) positioniert. Für die Targets wurden Bestrahlungspläne mit einer vorgeschriebenen

Dosis von 100, 200 und 500 cGy erstellt. Das Bestrahlungsplanungssystem berechnete die zu erwartende Dosisverteilung und die erforderliche Bestrahlungszeit für den Photonenstrahl.

Zur Validierung der Vorschreibungen wurde die Abweichung von der berechneten Dosisverteilung ermittelt. Die Dosis wurde im Kleinfelddosimetrie-Phantom mit dem microDiamond Detektor gemessen. Die beste Übereinstimmung wurde für den Kollimator mit 8 mm Durchmesser gemessen, der auch für das Referenzfeld des Beam-Modells verwendet wurde. Für diesen Sekundärkollimator wurden insgesamt 10 Behandlungspläne mit einer maximalen Abweichung von unter 2% validiert. Für die größeren Sekundärkollimatoren wurde die Dosis vom Planungssystem um bis zu +8,8% für den 30 mm Kollimator und um +5,9% für den 15 mm Kollimator zu niedrig prognostiziert. Die größten Abweichungen wurden für den 5 mm Sekundärkollimator festgestellt. In 50 mm Tiefe wurde -10,2% Dosisabweichung gemessen.

Bei Betrachtung der gemessenen Tiefen lagen die mittleren relativen Abweichungen zwischen -0,7% und +2,2%. Die höchste durchschnittliche Abweichung von +2,2% wurde bei den oberflächennahen Messungen in 3 mm WED festgestellt. Die beste Übereinstimmung mit -0,1% mittlerer relativer Abweichung wurde für die Werte in 11 mm WED ermittelt.

Die Abweichung des kleinsten Sekundärkollimators verdeutlicht die Bedeutung der Positionierung. Der derzeit verwendete Positioniertisch ist jedoch in seiner Stabilität begrenzt, was zu einer geringeren Genauigkeit führt. Daher ist die Entwicklung einer verbesserten Version des Tisches vorrangig, um die Präzision und Zuverlässigkeit zu erhöhen.

6

Inhaltsverzeichnis

Inhaltsverzeichnis

8

1 Introduction

According to the World Health Organisation (WHO), cancer is a leading cause of death worldwide and is responsible for nearly one in six deaths [1]. The cancer statistics of the International Agency for Research on Cancer (IARC) GLOBOCAN count 19.3 million new cancer cases and 10 million cancer deaths worldwide for the year 2020. For the year 2040, 30.2 million new cases are estimated. The rising trend underscores the need for broad access to cancer treatment, as well as the development of new treatment approaches [2].

Cancer cells are able to invade surrounding tissues or spread to distant parts of the body (metastasis), affecting the ability of cells and tissues to function normally. There are different treatment approaches with individual benefits for each patient. The three main pillars of cancer treatment are surgery, radiotherapy, and systemic therapy [1, 2].

In order to investigate the safety and efficacy of novel therapies, pre-clinical research involves a range of techniques and methods. In-vitro models, provide biomedical information by imitating the characteristics of cells in the tissue. The models improve the understanding of molecular mechanisms such as tumour growth, metastasis, drug resistance and aspects of immune evasion. In cancer research, in-vitro cancer studies are routinely performed with monolayer cultures under 2-dimensional conditions. The advantage is ease and low cost of maintenance, but these models are mainly seen as a highly simplified version of tumour conditions. 3-dimensional in-vitro models are considered more realistic. They better represent tumour growth, metabolism, cell-cell interactions and the tumour microenvironment. Appropriate in-vitro models should always be used to their maximum potential first, before studies in animal models. In-vivo research bridges the gap between in-vitro cell experiments to clinical applications [2–6].

Compared to radiation therapy (RT) for humans, small animal research requires sub-millimeter precision, which delayed the development of adequate systems. However, with the commercialisation of specialised radiation equipment, image guided radiotherapy systems have been increasingly integrated into pre-clinical research over the last decade [7, 8].

To develop image guided irradiation of small animals with ion beams and photon beams, the Department of Radiation Oncology at the Medical University of Vienna is currently collaborating with the MedAustron Ion Therapy Centre (Wiener Neustadt, Austria) and the University of Applied Sciences Wiener Neustadt (Wiener Neustadt, Austria). The synchrotron center MedAustron was not designed for the irradiation of small animals, so to meet the irradiation needs of small animals the infrastructure of the dedicated research room requires adaptation and

expansion. In addition, a special workflow must be created for the treatment of small animals, which should be comparable to the workflow for the treatment of patients. An X-ray irradiation unit will be used as reference irradiation system. Therefore, a setup was developed in previous projects [9, 10]. The setup consists of an X-ray tube, a beam collimation system, a movable table and couch for positioning of the anaesthetised small animal and a small field dosimetry phantom (SFDP) for dosimetric measurements.

In this project, a beam model for the reference irradiation device was created in μ-RayStation 8B (RaySearch Laboratories, Stockholm, Sweden), a treatment planning system (TPS) specially developed for small animal irradiation. The first step was to determine which definitions were required for the creation of the model. The tube was specified with the import of the energy spectrum and the measurement of the dose rate for the reference field at the reference point. For the secondary collimators (SCs), depth dose profiles (DDPs) and lateral dose profiles (LDPs) were measured and the corresponding field sizes determined. The measurement data for the characterisation of the photon beam (X-ray) was imported into the TPS and the beam model was commissioned. For the validation, dedicated dosimetric measurements were executed.

2 Physical and Technological Background

In the following sections an overview of the physical and technological background is given. Section 2.1 gives an introduction to the development of radiation therapy and presents its current status, followed by an introduction to pre-clinical research. The interaction processes of photons and ions with matter are explained in sections 2.3 and 2.4. Section 2.5 and section 2.6 describe the functionality of dose detectors and X-ray tubes. The last section 2.7 summarises different mechanisms for dose calculation techniques.

2.1 Radiation Therapy

Almost immediately after the discovery of X-rays by Röntgen in 1895, the use of ionising radiation on cancer patients started [11, 12]. Most external radiotherapy was performed with X-rays up to 300 kVp until about 1950. The kilovoltage devices used in the 1950s and 1960s gradually became less common as higher energy devices were developed and Cobalt-60 devices gained in importance. Even though megavoltage beams are usually used in radiotherapy today, lower energy beams have not completely disappeared. There are still certain applications for these devices, especially for the treatment of superficial skin diseases [13].

Nowadays, the main application for kilovoltage X-ray beams is imaging. After the discovery, the extraordinary potential of X-rays for diagnostic purposes quickly became clear. For many years, X-ray examinations were performed in a dark room by viewing images on a fluorescent screen that lit up in response to the X-rays that had penetrated the patient's body. It was not until 70 years after Röntgen's discovery that the development of the computer made technologies such as computed tomography (CT), magnetic resonance imaging (MRI) and interventional fluoroscopy possible [14].

Concerning radiotherapy, one main research pillar focuses on preserving healthy tissue surrounding the tumour. Individual treatment concepts are developed depending on the characteristics and location of the tumour. Ion beam therapy (IBT), due to the characteristic Bragg peak, enable a more targeted dose application in comparison to conventional photon RT (see section 2.4). This holds significant interest for targets in close proximity to dose sensitive organs. As shown in Figure 2.1.1, the dose deposition of the photon beam differs from that of the proton beam. While photons continuously deposit dose in the tissue, protons, as well as ions, follow the Bethe-Bloch equation (2.4.3) and deposit the highest dose at the end

11

of the range, described in detail in section 2.4 [15, 16]. Therefore, less energy is deposited in the surrounding tissue compared to photons. In Figure 2.1.1 also the spread-out Bragg peak (SOBP) is shown. By combining multiple ion beams with different energies, the dose distribution adds up and covers the tumour, while sparing the surrounding tissue [12, 16, 17].
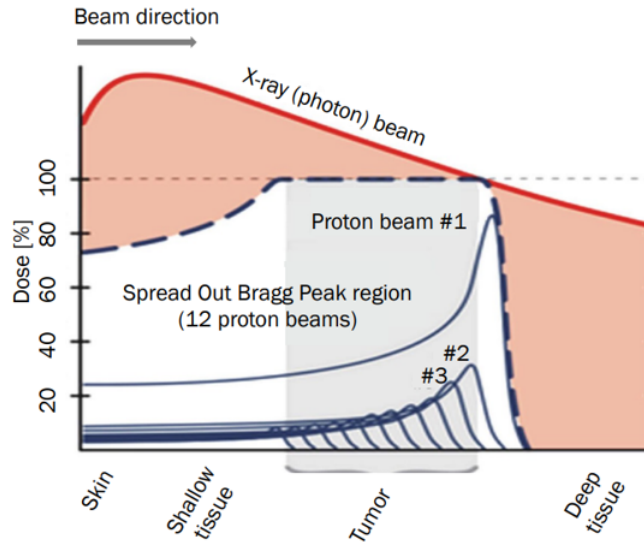

Abbildung 2.1.1: Comparison of photon and proton depth dose distributions [16].

According to the Particle Therapy Co-Operative Group (PTCOG), in 2021 world wide over 320,000 patients were treated with IBT, of which 280,000 were treated with protons and 40,000 with carbon ions [18]. The implementation of IBT was slow due to the significant technical challenges involved in its development in combination with the high construction costs. However, the number of treatments with IBT is increasing and with it the number of facilities. By 2021, 120 IBT facilities were in operation.

A major benefit of IBT is the higher biological efficiency, described by the relative radiobiological effectiveness (RBE). By using a weighting factor, the biological effect of ions compared to photons is taken into account for treatment planning. For two radiation modalities, the RBE defines the ratio of doses to reach the same biological effect

$$RBE(X) = \frac{D_{\text{reference}}(X)}{D_{\text{ions}}(X)}. \tag{2.1.1}$$

In IBT the dose is prescribed as Gy [RBE]. For example, in proton therapy, the RBE is considered to be a constant factor of 1.1. This value was derived as an average value of experimental cell data measured in-vivo, which were determined in the early days of proton therapy. However, more recent studies indicate a variable RBE that increases significantly towards the end of the proton range

[19]. The RBE of ions may be a complex function of numerous factors such as treatment technique, dose, cell type, intrinsic radiosensitivity, and the biological or clinical endpoint of interest. The use of a constant RBE can lead to suboptimal treatment outcome. A better understanding of the relationships between in-vitro, in-vivo and clinical RBE is needed to optimise treatment planning [20, 21].

2.2 Pre-Clinical Research

Pre-clinical research involves a range of techniques and methods used to investigate the safety and efficacy of novel therapies or therapy techniques. Pre-clinical studies can include in-vitro cell experiments or in-vivo animal models. The results of pre-clinical research serve as the basis for deciding, whether to conduct clinical trials in humans and help in the planning of these trials. In-vitro cell studies are one of the main pillars of cell and molecular biology. The models offer a wide range of applications, allow reproducible experiments and the maintenance costs are low. Applications are, for example, in basic cell biology research, viral biology, vaccine development and drug development. The creation of a defined cellular environment in which individual factors can be manipulated, provides the possibility to study cellular responses. In cancer research, cell lines improve the understanding of cancer development, growth, and drug resistance [3, 22]. In-vitro studies, as basic research, provide the information for deciding on further clinical development. Following successful in-vitro studies, in-vivo animal studies may be conducted to improve the transition from in-vitro cell trials to clinical application. The goal of pre-clinical research is to identify promising treatments that have the potential to improve treatment outcomes and reduce side effects [6, 23].

2.2.1 Pre-Clinical Animal Research

Animal studies are an important part of pre-clinical research, as they bridge the gap between in-vitro cell experiments and clinical implementation. The experiments study the fundamental characteristics of cancer, for example tumour formation and growth, mechanism of metastasis, as well as physiological effects. Mice and rats are commonly used due to their small size, ease of handling and high reproductive rate [6]. However, animal studies are subject to strict ethical guidelines. According to the directive 2010/63/EU of the European parliament and of the council [24], it should be ensured that the chosen method gives the most satisfactory results and causes the least pain or suffering. Furthermore, the smallest possible number of animals should be used that would give reliable results. In the recommendation on guidelines for the accommodation and care of animals used for experimental and other scientific purposes [25], the commission of the European communities describes animal research as a conflict of interest between science and the needs of the animals, and demands that the physiological and ethological basic needs of the animals to be restricted only for the minimum time and extent necessary. The

animals must be properly cared for and housed, and specific guidelines are given for the different species.

Small animal models have potential advantages over cell studies for radiobiological studies of tumour and normal tissue response. A pre-clinical model allows the effects of radiation, including induced side effects, to be studied without confounding variables. They offer the possibility to validate in-vitro results, test tolerance doses and investigate fractionation effects and clinical efficacy. In addition, the availability of tissue histology provides information about the underlying cellular changes [26, 27]. Tumour models are used to evaluate how the new treatment affects the growth and progression of cancer. The models are mainly generated by xenotransplantation of human tumour material into immunodeficient mice or rats [6]. Transplantation into the back, flank or hind leg allows easy accessibility and thus easy monitoring of tumour growth. As there are usually no organs at risk (OARs) in the immediate vicinity, local irradiation can be carried out very easily and in therapeutically relevant doses. The results of animal studies are carefully analysed to determine, if the new intervention is safe and effective enough to proceed to human clinical trials [23, 28].

RT for humans includes three-dimensional (3D) treatment planning as well as image-guided, conformal, precise beam application, but animal research lags behind. As the entire geometry has to be reduced, positioning of the animals and dosimetry has to be performed with increased accuracy. To achieve sub-millimeter accuracy, special setups and collimator techniques must be used. Recently, the development of special irradiation equipment for small animals has gained considerable attention as ultrasound, CT, MRI and positron emission tomography (PET) have been commercialised for small animals [6]. Treatment planning is also a challenge, because of the higher resolution of the images and the small beam sizes of down to 10 mm [29]. The aim is to mimic the classic clinical RT workflow including the following steps: planning CT acquisition, segmentation of planning CT in tissues, contouring of target and OARs, plan creation, accurate dose calculation, plan analysis and dose delivery [6, 17].

In collaboration with the MedAustron Ion Therapy Center (Wiener Neustadt, Austria) and the University of Applied Sciences Wiener Neustadt (Wiener Neustadt, Austria), the Department of Radiation Oncology at the Medical University of Vienna is currently working on establishing the technological basis for image-guided irradiation of small animals with ion beams and X-rays. A setup for an X-ray irradiation unit for a 200 keV photon beam (YXLON Maxishot, YXLON GmbH, Hamburg, Germany) was developed, which will be used for reference irradiation.

2.2.2 X-rays as Reference in Pre-Clinical Research

Given that RT has been practised since shortly after the discovery of X-rays, photon therapy has been extensively researched and its effects can be reliably predicted due to its linear progression. Nowadays, in RT kilovoltage X-ray beams are used for the treatment of skin lesions and superficial skin cancers [12]. For

use in animal research, X-ray devices offer the advantages of relatively simple radiation shielding, compactness, safety and ease of use. X-ray cabinet systems can be installed in a pre-clinical research area, allowing irradiation experiments to be performed independently of the clinical routine [30].

IBT, as well as photon beam therapy, is mainly based on an X-ray CT scan for treatment planning including dose calculation. The CT image data represents the density of the tissue and shows the relative inability of electromagnetic radiation to traverse a material. For IBT, the electron density must be converted into the relative stopping power for the ions. Accurate density information is crucial due to the higher sensitivity of the particle range and thus dose [17, 31]. Reference irradiation provides a basis for the correct calculation of the beam attenuation on the CT image.

The CT image represents a map of linear attenuation coefficients μ. The CT numbers normalised to the range from -1,000 for air to $+$ 2,000 for dense bone, while water is set to 0, are called Hounsfield units (HUs)

$$HU = \frac{\mu - \mu_{H_2O}}{\mu_{H_2O}} \times 1000, \qquad (2.2.1)$$

where μ is the linear attenuation coefficient. A HU represents a change of 0.1% in the attenuation coefficient of water [13]. For IBT, the HUs must be converted into stopping power using suitable calibration curves [17, 31].

The CT information forms the basis for the structure delineation, which is often supplemented by MRI or PET image information. The exact delineation of the surface contour, the internal structures and the target volume is not only crucial for the optimisation of the treatment, but also for the calculation of the dose distribution. The image segmentation and the treatment planning are described in more detail in section 2.7.

2.3 Interactions of Photons with Matter

As described in detail by Pawlicki et al. [12], when a photon beam penetrates a material, the photons have chances for three different outcomes. First, the photon transmits without interaction. These photons are called primary photons and form primary radiation. Secondly, the photon is scattered during one or more interaction and form secondary radiation. The last option is absorption of the energy in the material.

The following equation (2.3.1) defines the ratio of photons transmitted through a material of thickness x, where I_0 is the incident number of photons, I is the number of photons transmitted and μ is referred to as the linear attenuation coefficient,

$$I = I_0 \cdot e^{-\mu x}. \tag{2.3.1}$$

The number of photons is reduced by various processes in which photons are absorbed or converted. The most important interactions are: coherent and incoherent scattering, photoelectric absorption, Compton scattering, pair production, and photodisintegration. In equation (2.3.2) the possibility of a photon traversing through a medium of thickness x without interaction is given. It is possible to split the coefficient of linear attenuation into different coefficients: ω for coherent scattering, τ for photoelectric absorption, σ for Compton scattering, κ for pair production and π for photodisintegration,

$$e^{-\mu x} = \left(e^{-\omega x}\right) \cdot \left(e^{-\tau x}\right) \cdot \left(e^{-\sigma x}\right) \cdot \left(e^{-\kappa x}\right) \cdot \left(e^{-\pi x}\right) = e^{-(\omega+\tau+\sigma+\kappa+\pi)x}. \tag{2.3.2}$$

Depending on the application, the equation can be simplified. Pair production and photodisintegration are negligible for a diagnostic photon beam, because the energy is too low, resulting in the simplified equation: $\mu = \omega + \tau + \sigma$. Therapeutic photon beams cannot interact by coherent scattering or photodisintegration, resulting in: $\mu = \tau + \sigma + \kappa$.

Figure 2.3.1 shows the importance of photoelectric, Compton and pair production interaction mechanisms depending on the energy level of the photon. For example, for soft tissue with $Z_{eff} = 7.4$, the probabilities of photoelectric and Compton interactions are equal at a photon energy of 35 keV [12].

Rayleigh (Coherent) Scattering

In coherent scattering, the photon is scattered by the atomic electrons. With no significant loss of energy the photon is scattered through the angle θ. The scattered X-rays have the same wavelength as the incident beam.

For RT applications, where high energy photons interact with low-Z tissue, this interaction is insignificant [13].
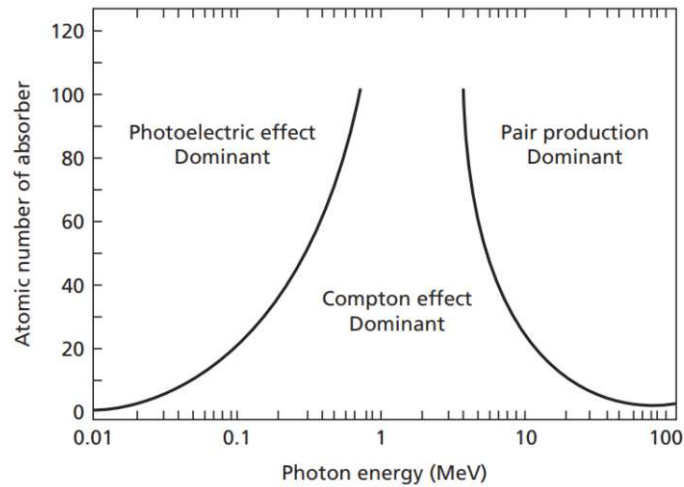
Abbildung 2.3.1: Relative importance of the photoelectric effect, Compton effect and pair production for interactions of photons in matter [12].

Photoelectric Absorption

In this process, shown in Figure 2.3.2, an atom absorbs the photon and ejects an inner-shell electron. The kinetic energy of the so called photo-electron results in $E_k = h\nu - E_b$, where $h\nu$ is the energy of the photon and E_b is the binding energy of the ejected electron. Cascading electrons fill the spaces left by the ejected electron, causing the emission of characteristic radiation and Auger electrons. These low-energy photons and electrons are absorbed in the surrounding tissue.
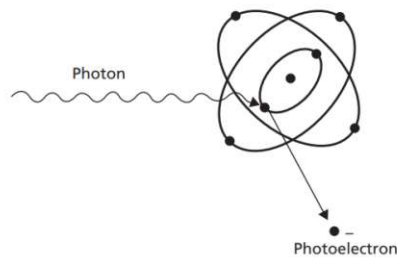

Abbildung 2.3.2: Schematic illustration of the photoelectric absorption in which the photon disappears and an inner-shell electron is ejected [12].

Photoelectric absorption is the most dominant interaction for low-energy X-rays, but the probability decreases rapidly with increasing photon energy [12].

17

Compton (Incoherent) Scattering

As shown in Figure 2.3.1, Compton interactions are the most dominant for X-rays with energies between 30 keV and 30 MeV. In the schematic illustration in Figure 2.3.3, a loosely bound or freeëlectron in the medium becomes a Compton electron, as the photon transfers part of its energy to the electron.
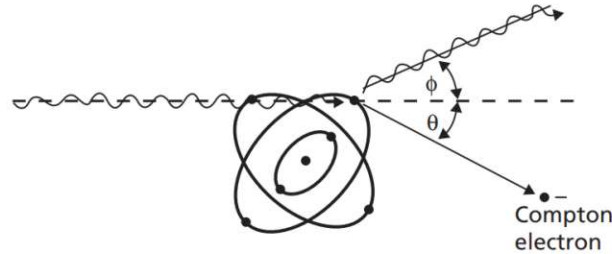

Abbildung 2.3.3: Compton effect of an incident photon ejecting a Compton electron. The photon is scattered at an angle ϕ and the Compton electron is ejected at an angle θ [12].

The incident photon with the energy $h\nu$ is scattered with the energy $h\nu'$ through a scatter angle ϕ

$$h\nu' = h\nu \left[\frac{1}{(1 + \alpha(1 - cos(\phi))} \right], \tag{2.3.3}$$

where $\alpha = h\nu/m_0 c^2$ and $m_0 c^2$ is the rest mass energy of the electron (0.511 MeV). The electron is set into motion with a kinetic energy E_k equal to the energy transferred and the electron scattering angle θ

$$E_\mathrm{k} = h\nu - h\nu' = h\nu \left[\frac{\alpha(1 - cos(\phi))}{(1 + \alpha(1 - cos(\phi))} \right]. \tag{2.3.4}$$

The wavelength λ' of the scattered photon is

$$\lambda' = \lambda + \Delta\lambda, \tag{2.3.5}$$

where λ is the wavelength of the incident photon and $\Delta\lambda$ is

$$\Delta\lambda = \lambda_c(1 - cos(\phi)), \tag{2.3.6}$$

where $\lambda_c = h/(m_e c) = 0.00243\ nm$ is the Compton wavelength with the electron mass m_e.

The transmitted energy is directly proportional to the change in wavelength. It is therefore greatest, when the change in wavelength is maximum at $\phi = 180°$. For low energy photons, most of the energy of the incident photon is retained by the

scattered photon and very little energy is transferred to the electron. This is in contrast to relatively high-energy photons, where only a small part of the energy is retained and most of the energy is released to the electron.

Due to the fact that Compton interactions occur with loosely bound electrons, the possibility depends directly on the electron density of the material. The formula for electrons per gram is given by ZN_A/M, where N_A is the Avogadro's number, Z the atomic number and M the atomic mass. From this formula, it follows how strongly photons in the tissue are attenuated by Compton interactions.

The attenuation of the photons leads to the optical density and thus to the contrast of an X-ray image. Different tissues can be distinguished in the image based on differences in optical density. These differences are collectively referred to as image contrast. Image contrast reflects differences in the transmission of X-rays through different regions of the patient. In RT, images are created with a low-energy diagnostic X-ray beam, which interacts mainly with photoelectric interactions. During the treatment, also a localisation image is created using the high energy treatment beam to check the alignment of the treatment beam. This verification image has a much lower contrast compared to the diagnostic beam. This effect is due to the different interactions of the beams. The therapeutic X-ray beam interacts almost exclusively by Compton interaction, resulting in noise on the detector due to scattered X-rays [12].

Pair production

This interaction occurs above a threshold energy of 1.02 MeV near an atomic nucleus. The photon is converted completely into an electron-positron-pair. The rest mass energy of an electron is equivalent to 0.51 MeV, therefore a minimum energy of 1.02 MeV is required for this interaction. The photon energy exceeding this threshold is shared between the particles as kinetic energy

$$(E_k)_{e-} + (E_k)_{e+} = h\nu - 1.02 \, MeV, \tag{2.3.7}$$

where $(E_k)_{e-}$ and $(E_k)_{e+}$ are the energies of the electron and the positron and $h\nu$ is the energy of the incident photon. Energy transferred to the nucleus can be neglected. Both, the positron and the electron, deposit energy on their way, as they interact as secondary particles. The positron merges with an electron, once it has used up all of its energy. Two photons are ejected at 180° to one another, each with energy 0.51 MeV [12, 13]. The mass attenuation coefficient for pair production increases almost linearly with the atomic number of the tissue. Also for photons above the threshold energy of 1.02 MeV it slowly increases with the energy. In high-energy radiotherapy, pair formation is a significant interaction. Unlike diagnostic radiology, as X-rays do not have enough energy for this type of interaction [32].

Photodisintegration

Tissue is rarely subject to photodisintegration, but shielding materials for high-energy accelerators are. When constructing shielding for linear accelerators that generate photons with an energy of more than 10 MeV, the generation of neutrons due to photodisintegration becomes a problem. For photodisintegration, photons need enough energy to eject a nuclear particle when they are absorbed by a nucleus. The photon is absorbed and either a neutron or a proton is ejected.
This interaction can be used to measure the energy of photons in a high-energy X-ray beam [12].

2.4 Interactions of Charged Particles with Matter

As charged particles travel through matter interactions with nuclei can occur, but most interactions are with the electrons surrounding the nucleus.
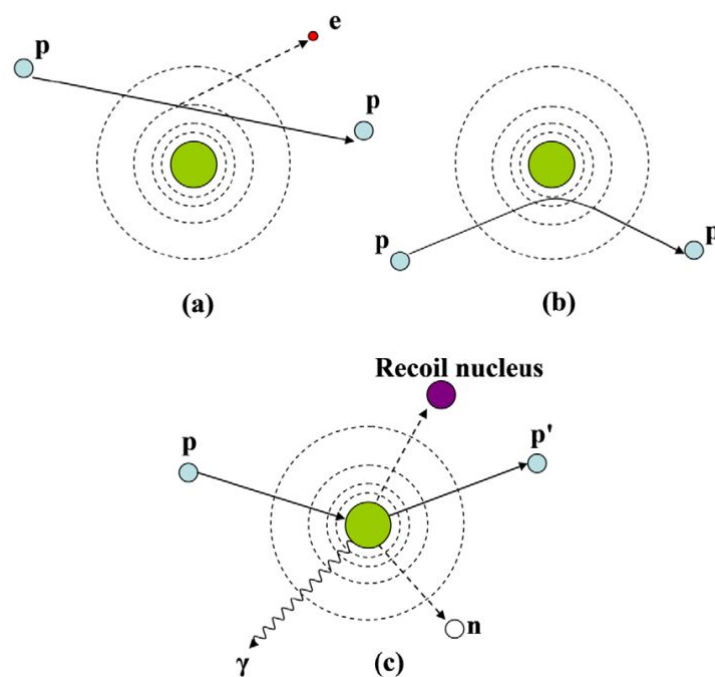

Abbildung 2.4.1: Schematic illustration of proton interaction mechanisms. Following interactions dominate: (a) Coulomb interactions with atomic electrons, (b) Coulomb interactions with the atomic nucleus, (c) nuclear reactions and bremsstrahlung [33].

In Figure 2.4.1 the dominant interaction mechanisms in particular for protons are shown. Despite the Coulomb interactions with electrons, most protons travel in a

nearly straight line, as illustrated in Figure 2.4.1 (a). This is because their rest mass is much higher, yet they continuously lose kinetic energy. By passing close to the atomic nucleus protons experience a repulsive elastic Coulomb interaction. As shown in Figure 2.4.1 (b) a deflection of trajectory is possible. A non-elastic nuclear reaction leads to a removal of a primary proton and creation of secondary particles. Figure 2.4.1 (c) illustrates a nuclear reaction in which the proton enters the nucleus and secondary particles are emitted: proton (p), electron (e), neutron (n), gamma rays (γ). For therapeutic proton beam energies, bremsstrahlung is negligible [33].

The energy loss of ions per unit path length is defined by the stopping power S

$$S = -\frac{dE}{dx}, \tag{2.4.1}$$

where E is the mean energy loss and x is the distance.

The total mass stopping power S_{tot} is given by the sum of the radiative and the collision stopping power

$$S_{\text{tot}} = S_{\text{rad}} + S_{\text{col}}, \tag{2.4.2}$$

where S_{rad} is the radiative stopping power resulting from Coulomb interactions with the nuclei of the absorber and S_{col} is the collision stopping power, resulting from Coulomb interactions with orbital electrons [34].

The energy loss is mainly caused by excitation and ionisation of atomic electrons. This is described by the Bethe-Bloch equation

$$\frac{S}{\rho} = -\frac{\mathrm{d}E}{\rho\mathrm{d}x} = 4\pi N_A r_e^2 m_e c^2 \frac{Z}{A}\frac{z^2}{\beta^2}\left[\ln\frac{2m_e c^2\gamma^2\beta^2}{I} - \beta^2 - \frac{\delta}{2} - \frac{C}{Z}\right], \tag{2.4.3}$$

where following variables are defined by the absorbing material: ρ is the mass density, I is the mean excitation potential, Z and A are the atomic number and the atomic weight. It is convenient to express the energy loss rate independent of the mass density. Furthermore, N_A is the Avogadro's number, r_e and m_e are the radius and the mass of an electron and z is the charge of the projectile. The Lorentz factor $\gamma = (1-\beta^2)^{-1/2}$ is dependent on $\beta = \frac{v}{c}$, where c is the speed of light and v is the velocity of the projectile. The last two terms are correction terms. They involve relativistic theory and quantum mechanics and need to be considered at very high or very low energies. δ defines density corrections arising from the shielding of remote electrons by close electrons and will result in a reduction of energy loss at higher energies. C is the shell correction term, which is only relevant for low energies [33, 35].

As can be seen from the Bethe Bloch equation (2.4.3), the energy loss of ions is proportional to the inverse square of their velocity. The slower the ion, the higher the energy deposition. The peak of radiological dose of ions is greatest near the end of their range, named the Bragg peak [15]. This effect is illustrated in Figure 2.4.2.
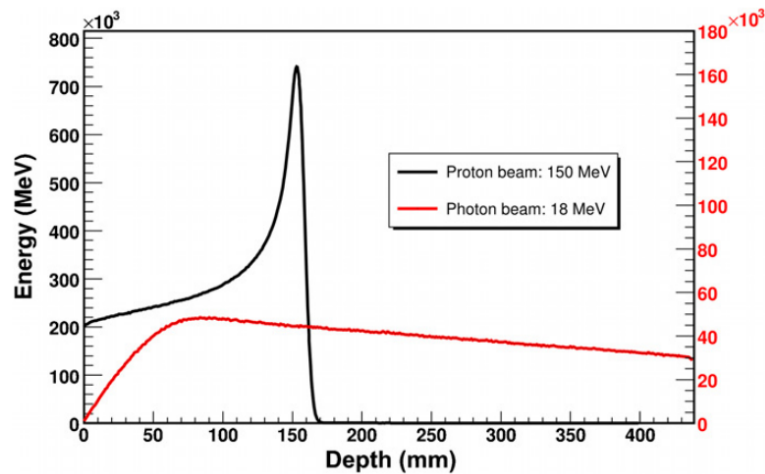
Abbildung 2.4.2: Energy deposition of a proton and a photon beam as a function
of depth [36].

Furthermore, the Bethe Bloch equation (2.4.3) shows that the rate of energy loss
is directly proportional to the atomic number Z of the absorbing material. Thus,
the penetration depth of the ion depends on the beam energy and the energy loss,
which in turn depends on the electron density of the tissue traversed.

In the human body, the density varies by about three orders of magnitude, from
the air in the lung to the cortical bone, which means that the linear stopping
power for proton energies between 1 and 250 MeV varies by a factor of about 60
[33, 37].

2.5 Dosimetry

The dose is probably one of the most important physics parameters in the treatment
of cancer. Dosimetry is the determination of radiation dose by measurement,
calculation or a combination of both. In general, a detector is a device that
responds to radiation depending on the amount of energy absorbed. Radiation
treatment is always about delivering the highest dose to the cancerous area and
sparing the normal tissue. To achieve this goal, the dose determination must be
very accurate and the detectors must be selected to suit the application [38].

For a precise dose delivery in IBT, the calibration of the therapeutic beam is
crucial. The amount of delivered particles is controlled by the beam monitor. For
IBT centers with an active scanning delivery technique, the monitoring system is
calibrated in terms of particle number or the equivalent energy deposition [39]. The
standards for reference dosimetry of clinical ion beams are given in the TRS-398
report [40]. Dosimetric measurements were required in this study to create the
beam model in the TPS, as well as to verify it.

2.5.1 Ionisation Chambers

Ionisation chambers measure the effects occurring, when a charged particle passes through a gas. Neutral molecules of the gas are ionised, and the resulting ion and electron, are called an ion pair. An external electric field conducts the charged particles to anode and cathode, which produces an electric current. When a given volume of gas is exposed to steady-state irradiation, the rate of ion pair formation is constant. The number of ion pairs correlates with the irradiation energy [41]. Parallel plate chambers are therefore essentially plate capacitors. As shown in Figure 2.5.1, the collecting electrode (C) of the chamber is surrounded by an annular guard electrode (G) and separated from it by an insulator. The guard electrode fulfils two important tasks. Firstly, the guard ring ensures that the electric field lines remain straight near the edge of the collecting electrode. Secondly, it minimises the extent of charge leakage from the volume. A voltage is applied across the thin window and the collector to measure ion pair production [42].
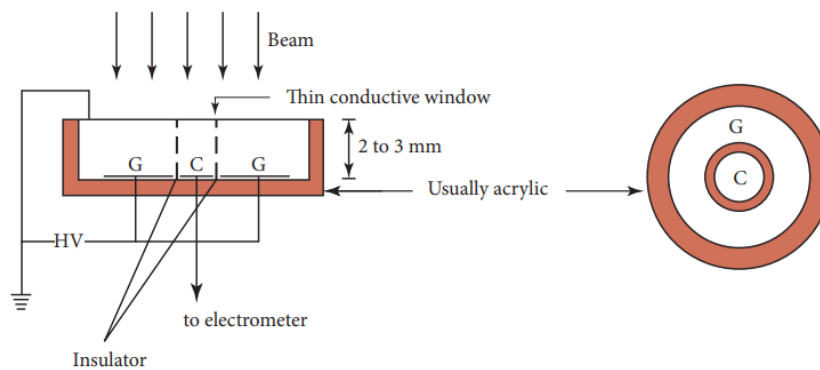

Abbildung 2.5.1: Schematic illustration of an ionisation chamber [42].

For an accurate measurement, it is necessary that the gap between entrance window and collecting electrode is parallel. If the distance between the electrodes varies, a homogeneous response behaviour cannot be achieved.
In the TRS-398 report [40], the calibration methods of cylindrical ionisation chambers in a ^{60}Co beam are described. Plane-parallel ionisation chambers are used for relative and reference dosimetry purposes. The energy deposition is defined as dose-area-product to water (DAP_w) [39, 43].

2.5.2 Diamond Detectors

Diamond detectors are solid state detectors made of carbon. The main advantage of diamond detectors is, due to their very small active volume the detectors have high spatial resolution, which leads to the ideal detector for small field dosimetry. They have an immediate dose response, are reliable and near-tissue equivalent. The

crystal of a natural diamond has a large band gap of 5.47 eV. It can be operated as a simple conduction counter by applying electrical contacts to opposite faces of the crystal. For a stable response, pre-irridiation is recommended [38, 42].
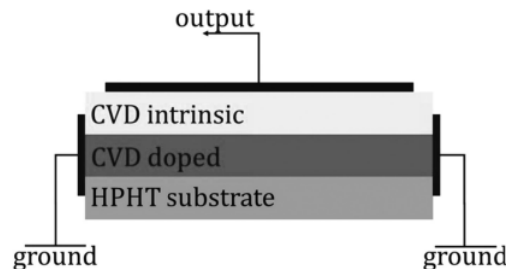

Abbildung 2.5.2: Synthetic single-crystal diamonds in a Schottky-diode configuration. The diamond consists of a film of CVD intrinsic diamond on a p-type doped CVD diamond and deposited onto a conductive HPHT substrate [38].

Today the crystal for detectors is artificially grown using the chemical vapor deposition process (CVD). A layer of intrinsic synthetic diamond is grown onto a doped surface. By evaporating an aluminum contact a Schottky-diode configuration is developed. Positive and negative charge carriers, created as a result of incident radiation, are separated by the diode's field. An electrometer can be used to measure the output signal [38].

2.5.3 Radiochromic Films

Radiochromic films are a common instrument for reference and relative dosimetry due to their ease of use and high spatial resolution. The films are layered with a radiosensitive dye of microcrystal monomers. In contrast to radiographic films, radiochromic films are self-developing. When exposed to radiation the dye is polymerised and changes to a bluish colour, reducing the light transparency. The structure consists of 1–2 sheets of polyester layers that contain 1–2 active layers. The density is nearly water-equivalent and the thickness differ between 10–90 µm. Radiochromic films show small dose rate and energy dependence. During the handling, gloves should be used, because oils on the skin/hands can affect the measurement of absorbance [12].
As for radiographic films, the dose is measured as optical density and absolute dose can be measured. For this purpose, each series of films must be calibrated for different dose levels that cover the range of use. From the resulting calibration curve, the deposited dose can be calculated based on the reaction of the film. The optical density is affected by a number of variables. This means that the structure of the scanning process, the film model and the dosimetry method result in a unique calibration curve [12, 38, 42].

2.6 X-ray Tubes

A schematic illustration of an X-ray tube is shown in Figure 2.6.1. The tube consists of a cathode (negative electrode) and an anode (positive electrode) evacuated to prevent interacting with gas molecules. The cathode consists of an assembly of a tungsten filament housed in a negatively charged focusing cup. Due to thermal emission, the cathode emits electrons when a current of few amperes heats the filament. The anode consists of a copper rod and a tungsten target. Tungsten is common as target material due to the high atomic number and the high melting point. An applied voltage between the anode and the cathode leads to acceleration of the electrons towards the anode. The electrons hit the target of the anode resulting in the production of characteristic X-rays and bremsstrahlung. As the electrons hit the target, the radiation spread out in all directions. To obtain a usable beam, the beam is usually collimated [12].

Bremsstrahlung is released when electrons and atomic nuclei collide inelastically. The loss of kinetic energy is converted into bremsstrahlung. The probability varies with Z^2 of the penetrated medium. Therefore high Z targets are more efficient at producing bremsstrahlung [13]. The energies for characteristic X-rays are defined by the target material and are independent of the electron energies. The spectrum for characteristic X-rays reflects the binding energies in the K, L and M shells. The main peak of characteristic X-rays reveals electron transitions from the L to the K shell. The transition from the M to the K shell is shown by a second peak. The X-rays have in both scenarios energies below the K binding energies of the electrons in the target material [32].
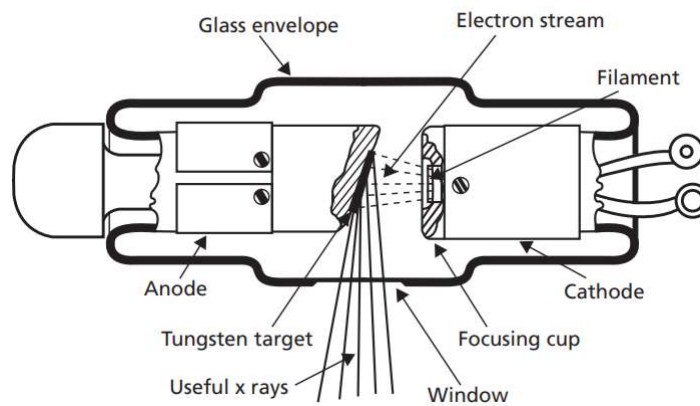

Abbildung 2.6.1: Schematic of an X-ray tube with a vertical beam [12].

The focal spot of an X-ray tube describes the volume in which electrons are absorbed and X-rays emitted. The smaller the target or filament, the sharper the beam [12]. When hitting the target, X-rays are generated at different depths of the target. This causes the intensity of the X-ray beam to vary, called the heel effect. The low X-ray energy and steep target angles of diagnostic tubes make this

impact more noticeable than with other imaging devices. Using a compensating filter to account for the heel effect and improve beam uniformity, can reduce this effect [13].

The tube current, voltage, and optional filters can be used to modify the resulting X-ray energy spectrum. The thermal emission of electrons is controlled by the filament current, which also regulates the fluence of the generated X-rays. The electrons maximal kinetic energy is determined by the tube voltage, which also defines the bremsstrahlung spectrum.

To optimise the beam for a specific application, filters can be placed in front of the exit window to absorb particular parts of the spectrum. For example, particular filters are inserted to harden the beam by absorption of lower energy radiation. These lower energies would be absorbed as patients dose without advantage for the treatment. In general filters decrease the total number of X-rays while raising their average energy in the beam [12].

The spectrum for the X-ray tube used in this study is shown in section 4.1.1 in Figure 4.1.1.

2.7 Treatment Planning

In the RT workflow, accurate dose prediction is one of the major challenges. Targeted treatment of the tumour requires the dose distribution to be precisely predetermined. The CT information forms the basis for the structure delineation, which is often supplemented by MRI or PET image information. The uncertainty of the calculated dose distribution depends on the quality of the CT scan and the accuracy of the dose calculation. It further requires accurate delineation of the structure, namely a correct determination of the target volumes and the delineation of OARs.

The target to be treated can be broken down into the gross target volume (GTV), the clinical target volume (CTV) and the planning target volume (PTV). The GTV is the macroscopic extent of the tumour visible in the planning images. The CTV includes the GTV plus a margin, that contains microscopic disease not visible. It depends on anatomical and tumour-specific growth and defines the volume to be irradiated with the prescribed dose. The PTV includes a margin around the CTV to account for patient setup inaccuracies and uncertainties in the beam delivery [12, 17].

After the structure delineation, the beam directions and beam aperture design are selected. An ideal treatment plan should, by definition, spare all normal tissues while delivering a tumour-killing dose to the entire tumour. During the iterative optimisation process, beam weights and positions are defined based on given beam directions and potential passive elements in the beam line. The use of multiple irradiation fields saves the surrounding tissue, as the dose is distributed over a larger volume outside the target [13]. Depending on the type of radiation, the dose distribution is calculated using different methods, including the pencil beam,

the convolution-superposition and the Monte Carlo method. The decisive factor for the choice of method is the trade-off between accuracy and calculation time. The calculation results in a 3-dimensional dose distribution [12, 32].

2.7.1 Dose Calculation Techniques

Ray Tracing Method

The beam is split into straight lines (rays) from the source trough the patient tissue. The dose deposition is calculated using depth dose curves measured along the central axis of broad beams located at selected depths below the surface. This method is very fast but has only limited accuracy, especially for lateral scattering processes. It is no longer used clinically [12, 17].

Pencil-beam Method

The pencil beam algorithm offers a good compromise between accuracy and computational speed. As shown in Figure 2.7.1, the treatment beam is split into elementary pencil beams, which are thin beams that are specified at the plane of final collimation [12]. The method is based on the translation of a heterogeneous patient tissue into a patient-specific water-equivalent system from the perspective of the beam. From the X-ray CT image of the patient, the depth scaling of the beam range is performed. The resulting dose is calculated from the superposition of all partial beams. Since only the inhomogeneities on the central axis can be taken into account, the agreement is not satisfactory for large density differences [12, 17, 32].
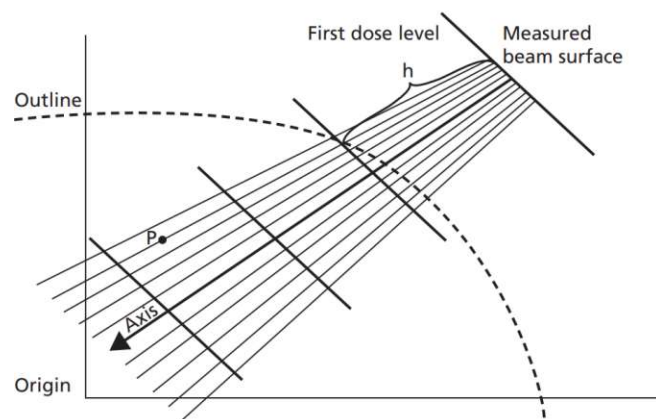

Abbildung 2.7.1: Schematic illustration of the pencil-beam method. The beam is split into elementary pencil beams. The deposited dose is calculated on the central axis [12].

Convolution-superposition Method

For the convolution-superposition method, for each energy component of the incident photon spectrum a separate calculation is performed and then summed over the spectrum. This procedure is time consuming, leading to several methods to speed up the calculation. In one method, the convolution is reduced to a product by the use of Fourier transformations. In a pure convolution calculation, the dose-spread array is independent of location, but once the dose-spread array has been averaged over the photon energy spectrum, it is no longer location-independent. This technique is called the convolution-superposition method. As computing speed has increased, the algorithm have become practicable for routine clinical treatment planning [12].

Monte-Carlo Method

The Monte Carlo method is a powerful computational technique used to simulate the behavior of particles, including photons, as they interact with matter. It is commonly used in medical physics to model the interactions with human tissue for RT treatments and to calculate important parameters such as absorbed dose and energy deposition.

For photons, for example, the path of an individual photon through a medium is simulated using probabilistic methods. The photon is modelled as particle that interacts with the medium through various mechanisms such as scattering or absorption. The probability of each interaction is calculated based on the physical properties of the medium and the energy of the photon. Each photon is followed through the medium until it either leaves the medium or its energy is completely absorbed. Since the Monte Carlo calculations are derived from random events, the resulting dose has an associated uncertainty. By calculating a large number of interactions, it is possible to minimise the uncertainty in dose [12, 32]. It is recommended to reach an uncertainty limit of less than 2% [44].
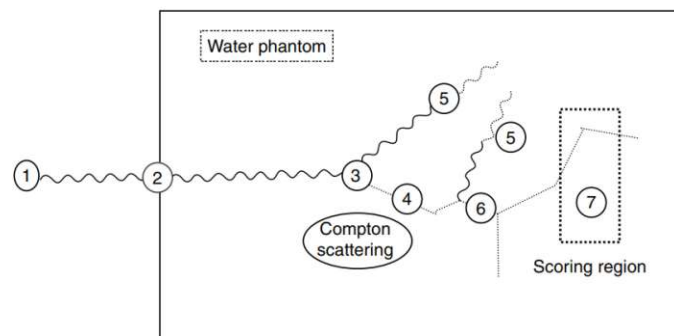

Abbildung 2.7.2: Schematic illustration of a Monte Carlo photon history [32].

Figure 2.7.2 shows the process of a Monte Carlo calculation with the following

steps:

1. Based on the distribution of the incident photons, the energy, the direction and the initial position of a single photon are selected

2. Define distance to the first interaction and transport the photon to this point

3. Choose the type of interaction: Compton scatter, photo-electric, pair-production or Rayleigh scatter

4. Choose directions, energies, etc. of the new particles and follow them as secondary particles

5. Transport scattered photon until it either leaves the geometry, or it gets absorbed

6. Transport secondary electron and keep track of any δ electrons and bremsstrahlung-photons produced

7. Score deposited energy, fluence spectra, etc. in the region of interest

8. Repeat steps 1–7 for more photons [32].

The result of the calculation is a 3-dimensional dose distribution grid of volume elements (voxels). The voxels contain the summed energy deposition of all calculations. Unlike other dose calculation algorithms, Monte Carlo calculations include the medium and the result is output as dose to medium. The deposited energy is calculated proportionally to the stopping power of the material in the voxel. In RT, dose is traditionally reported as dose to water. For therapy planning, the conversion from dose to medium to dose to water is needed [12, 45, 46]. In Monte Carlo calculations the computation speed is still an issue. For faster approximations, the so-called physics list limits the choice of interactions. The list indicates the type of particles, the physical processes they undergo and the production thresholds. The processes are adapted to the application and the energy ranges. As the list of physical processes for realistic applications becomes quite long, the systems usually include modular physics lists. These lists contain major interactions for certain applications, for example electromagnetic physics, hadronic physics or optical physics [47–49].

The Monte Carlo method is very accurate, but computationally intensive, therefore it is not yet used for routine photon beam treatment planning. Since the convolution-superposition method is also very accurate for photons, it is not required for most indications.

3 Materials and Methods

The following sections report on the utilised materials and methods for this study. Section 3.1 introduces the MedAustron Ion Therapy Center (MedAustron). In section 3.2 the measurement setup and the used dosimetry equipment are described. The last section 3.3 explains the TPS µ-RayStation and the creation of the beam model.

3.1 MedAustron Center for Ion Beam Therapy and Research

The MedAustron is a facility for ion beam therapy (IBT) and research located in Wiener Neustadt, Austria. It is in operation since 2016 and today offers three irradiation rooms (IRs) for clinical treatments and one IR for non-clinical research purposes, as can be seen in Figure 3.1.1. Both the research IR and the treatment IR3 are limited to a horizontal beamline. The IR2 has a vertical and a horizontal beamline, while IR4 is equipped with a proton gantry.

Abbildung 3.1.1: Schematic of the MedAustron facility. IR1 is for non-clinical research. IR2, IR3 und IR4 are for patient treatment either with protons or carbon ions [50].

At present, protons and carbon ions are used for treatment. They are pre-accelerated in a linear accelerator (linac) and then injected into the synchrotron

(circular accelerator). In the medical field, the energy range for protons is 60 to 250 MeV, for carbon ions between 120 and 400 MeV per nucleon. For research, proton energies up to 800 MeV are available [50]. As reported by the PTCOG in the patient statistics for 2021, a total of 1034 patients were treated with protons and 227 patients with carbon ions at the MedAustron [18].

With the multi-ion facility, it is also possible to expand to other types of particles, for example to explore the application of helium ions. For research projects on the further development of particle therapy, the MedAustron is internationally networked with clinics, universities and research institutes [50].

3.2 Reference X-ray Setup

The reference X-ray setup comprises the X-ray cabinet unit and the measurement setup. The measurement setup includes the beam collimation system, the positioning table and couch and the small field dosimetry phantom (SFDP), which is equipped with RW3 plates. The measurement setup is placed inside the X-ray unit. A microDiamond detector and EBT3 Radiochromic films were used for dosimetric measurements.

3.2.1 X-ray Unit

A commercially available YXLON Maxishot X-ray cabinet unit, developed by YXLON International GmbH (Hamburg, Germany), is used as X-ray reference system for pre-clinical IBT research. The X-ray tube is an oil cooled type Comet Y.TU/320-D03. It is mounted on the side of a steel container providing a horizontal beam. The exit window has a diameter of 120 mm. The steel container is equipped with height adjustable rails (20 mm steps) that can be used to attach experimental setups. The target material is tungsten and the target angle is 20°. The focal size can be switched between 3.0 mm and 5.5 mm. The Y.TU/320-D03 tube includes three different filters 3.0 mm Beryllium, 3.0 mm Aluminium and 0.5 mm Copper, whereas the Beryllium filter is fixed, the Aluminium filter is removable and the Copper filter is an accessory pack. An external control unit is used to change the voltage, current, time, and focus size. The irradiation time can be changed in steps of one second. The maximum tube current is 21 mA and the accelerating voltage is limited to the range of 15 to 200 keV [30]. In this project, all measurements were performed at the maximum voltage of 200 kV, a focal spot of 5.5 mm and a tube current of 20 mA. The energy spectrum was calculated using the software SpekCalc (version 1.1) and is shown in section 4.1.1 in Figure 4.1.1 [51].

3.2.2 Measurement Setup
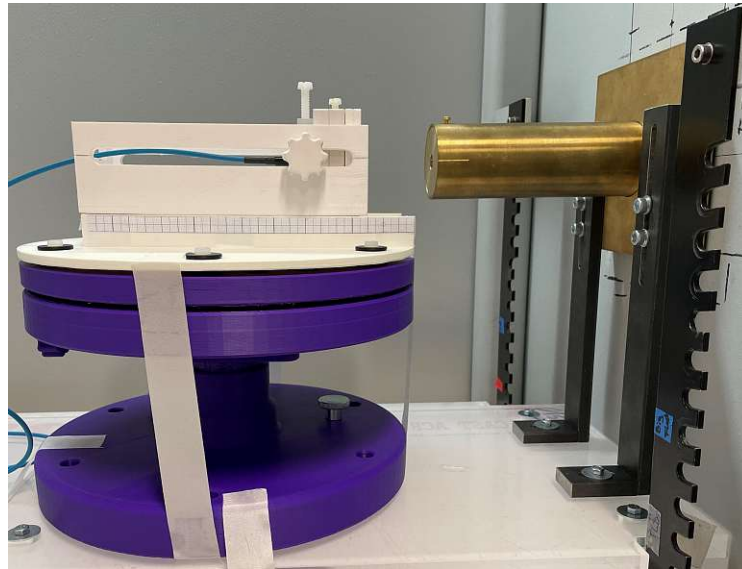
(a)
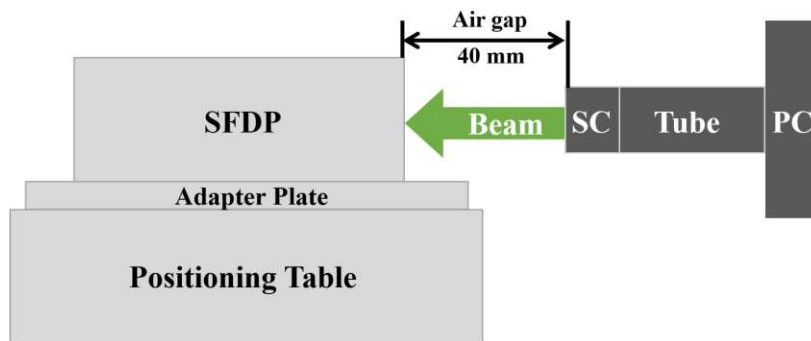
(b)

Abbildung 3.2.1: In (a) an image of the measurement setup and in (b) a schematic is shown. It consists of the X-ray positioning table, an adapter plate for the SFDP or the couch, the collimator system with primary collimator (PC) and secondary collimator (SC) and the SFDP, mounted on acrylic glass (Plexiglas) plates on the rails of the X-ray unit.

The setup, shown in Figure 3.2.1, consists of a positioning table, an adapter plate for the SFDP or the couch for the small animal and the beam collimation system. The setup was positioned on acrylic glass (Plexiglas) plates on the rails of the X-ray unit. The table was 3D printed out of Polylactide (PLA) and has inserts for the adapter plate, which can be adjusted for the SFDP or the couch. The

couch was developed for the fixation of anaesthetised mice during irradiation and provides space for cables for anaesthesia, as well as breathing and temperature monitoring. The couch is compatible with the CT scanner, enabling consistent positioning for imaging and irradiation. The positioning table provides adjustable positions with three translational and one rotational degrees of freedom [9]. In the measurements for this project, the setup was always in the fixed position shown in Figure 3.2.1 (a). The SFDP was positioned directly and straight in front of the beam exit. The SFDP was equipped with RW3 slabs in the size 60 mm × 60 mm in different thicknesses of 1 mm, 5 mm or 10 mm. RW3 is a water equivalent material (water equivalent depth (WED)) and is often used for solid state phantoms [52]. Additionally, the SFDP includes holders for the microDiamond detector (PTW-Freiburg, Germany) and the Advanced Markus chamber (PTW-Freiburg, Germany).

Due to its original development for industrial purposes, the uncollimated photon beam of the X-ray unit has a minimum diameter of 120 mm, which is too wide for effective use in small animal research without collimation. In a previous study [10], a beam collimation setup was designed and manufactured to collimate the beam to a circular field size with diameters between 5 mm and 30 mm. The collimator structure contains the PC, fixed to the acrylic glass plates. The SCs can be inserted into the primary and currently there is a set of 8 different apertures between 5 mm and 30 mm available (diameters: 5 mm, 7 mm, 8 mm, 10 mm, 15 mm, 20 mm, 25 mm, 30 mm). In this study, the SC with 8 mm diameter defined the reference field. The SFDP was placed on the X-ray positioning table using the adapter plate and the air gap between the SFDP and SC was adjusted by moving the SFDP within the guides of the positioning table. In this study, all measurements were conducted with 40 mm air gap between the surface of the SFDP and exit of the SCs, as shown in Figure 3.2 (b).

3.2.3 EBT3 Radiochromic Films

GAFchromic$^{\text{TM}}$ EBT3 films (Ashland Inc., Bridgewater, NJ) were used for dosimetric measurements. The films are made of two symmetric matte polyester layers that are each 125 µm thick, sandwiching a sensitive monomer layer with a thickness of 28 µm. The films of lot # 03122003 were used for the evaluation of LDPs and were cut into pieces of 60 mm × 60 mm for the SFDP. The films had the same size as the water equivalent RW3 slabs for the SFDP and were sandwiched in between. The vendor recommends a dose range for EBT3 films from 0.1 cGy up to 10 Gy [53, 54]. In the measurements for this project, the films were always irradiated for 180 seconds, which corresponds to doses between 200 cGy and 650 cGy. An Expression 11000XL flatbed scanner (Seiko Epson Corporation, Nagano, Japan) was used for film scanning. The films were scanned 24 to 48 hours after irradiation. Prior to scanning, five scans without films were performed, to account for warm-up effects of the scanner. Each scan was conducted in portrait orientation (long side of the film parallel to scanning direction) and a template

was used to align the film segments with the scanner's center reference point, to minimise lateral scanning artefacts. The professional mode of the Epson Scan software was used and all imaging adjustments and color corrections were disabled. As resolution 150 dpi was set. Each film was scanned three times and the images were saved in 48 bit RGB uncompressed tagged image file format (TIFF). The film scans were read and processed using the programming language Python (version 3.9) [55]. The scanned image consists of three color channels of each 16 bit color depth. For all analyses in this study, only the red color channel was considered, as common in film evaluation [56, 57].

The optical density

$$OD = log(I_0/I) \tag{3.2.1}$$

describes the opacity of the film. I_0 is the incident light intensity and I is the light intensity passing through the film. For a transmission scan with 16 bit color depth for each color channel, the optical density is

$$OD = \log \frac{PV_0}{PV + 1}, \tag{3.2.2}$$

where $PV_0 = 2^{16}$ is the maximum pixel value (PV). The OD_{net} is described by the difference in optical density of a non-irradiated (background scan) film OD_{bkg} and after irradiation with a dose OD_{irr}

$$OD_{net} = OD_{irr} - OD_{bkg} = \log \frac{PV_{bkg} + 1}{PV_{irr} + 1}. \tag{3.2.3}$$

The optical density OD_{net} was used to evaluate the dose response [56, 58].

The films were scanned three times and the PVs averaged. The PVs were then converted into absorbed dose by using a calibration curve. A calibration curve must be created for each set of films. The calibration curve for 200 keV X-rays, using the presented X-ray unit, was determined in [10]. This was done by exposing the films to defined dose levels between 0 and 11 Gy and determine the optical density. The curve was created by fitting a 4th order polynomial to the dose response curve.

The resulting 2-dimensional dose image was divided into dose lines. The lines were summed and the line with the highest value contains the center point of the field. From this point the dose was read inline (vertical) and crossline (horizontal). The dose line defined the LDP of the collimated beam. By measuring the width to 50% dose fall off, field sizes of the SCs were determined [32].

3.2.4 MicroDiamond Detector

The microDiamond detector PTW-60019 (PTW, Freiburg, Germany), shown in Figure 3.2.2, is a synthetic single crystal diamond detector (SCDD) for radiation dosimetry applications. It is disk-shaped, waterproof and has a sensitive volume perpendicular to its detector axis. The sensitive volume is 0.004 mm³ within a

radius of 1.1 mm and thickness of 1 µm. The measuring quantity is absorbed dose to water in a nominal response of 1 nC/Gy. The so-called reference point is located on detector axis, 1 mm from the detector tip and is marked by a ring. The detector has an entrance window with a water equivalent thickness of 1 mm (1 mm WED). It is recommended to pre-irradiate the detector with a dose of 5 Gy. According to the manual [59], measurements can be performed in an energy range between 100 keV and 25 MeV for field sizes down to 10 mm × 10 mm.

As already described in section 2.5.2, synthetic diamond detectors work as a Schottky diode and should be operated at 0V external detector bias. Incident radiation generates charge carriers which are separated by the field of the diode and were measured with a PTW UNIDOS[webline] electrometer [59].

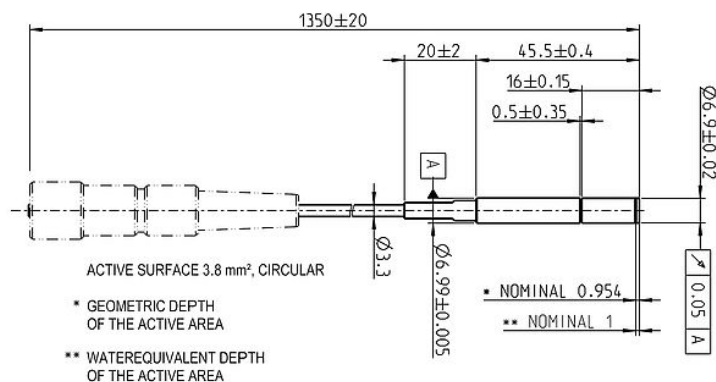The microDiamond detector was used for the measurement of DDPs.

Abbildung 3.2.2: Technical drawing of Type No. PTW-60019 microDiamond detector. Dimensions are given in mm [59].

3.3 Treatment Planning System: µ-RayStation

µ-RayStation 8B (RaySearch Laboratories, Stockholm, Sweden) is a TPS adapted for small animal research. The adjustments are necessary, because of the higher resolution of the images and thus a more detailed dose map. The TPS uses a Monte Carlo dose calculation engine that is adapted for small fields. The aim was to create a beam model to provide a basis for the correct calculation of the beam attenuation on the CT image.

3.3.1 µ-RayPhysics

µ-RayPhysics is included in µ-RayStation 8B and is the main part for the creation of a beam model. All parameters for the characterisation of the beam were set or imported into this module of the TPS. The machine model consists of three

basic components: the X-ray source, the entrance collimator and the cones. The entrance collimator corresponds to the PC and the cones to the SCs of the setup. For the import of the LDPs and DDPs into μ-RayPhysics, the dose values were normalised to the maximum and imported with dedicated headers. The headers include following configurations: the source to surface distance (SSD), the radiation type (photon) and energy (0.2 MV), the field size, the curve type (crossline, inline or depth), the cone name and shape (circular) and the relative dose values. For DDPs, the header also contains the measurement medium (water). μ-RayPhysics linked the LDPs and DDPs directly to the previous defined SCs.

X-ray Source

For the definition of the source, the energy spectrum of the photon beam was imported. The spectrum was calculated using the software program SpekCalc with the properties of the X-ray tube, as described in section 3.2.1, including the peak energy, the target angle and the filters. The resulting energy spectrum was imported into μ-RayStation and is shown in section 4.1.1 in Figure 4.1.1 [51]. Required settings are the tube current, which is fixed to 20 mA, the steady dose rate and the half rise time. The steady dose rate was measured at the reference point for the reference field. It was defined as [MU/s] (monitor units per second) and 1 MU/s corresponds to 1 cGy per second measured in 10 mm WED. The dose rate was measured with the microDiamond detector in the SFDP in 10 mm depth of RW3. The half rise time was defined as time to reach half the steady dose rate. It was determined with an in-house developed software for the measurement of time-resolved dose.

Source to Axis Distance

The source to axis distance (SAD) defines the position of the reference point in relation to the focal spot of the X-ray tube. When selecting the position of the reference point, it was important to ensure that there is enough space to easily move and rotate the positioning table with an anaesthetised mouse. On the other hand, the reference point should be as close as possible to the beam exit, because of the rapid decrease of dose rate with increased distances. Based on these criteria, the reference point was defined at a distance of 50 mm after the exit of the SC. The SAD was defined as the distance from the focal spot to the reference point. As shown in Figure 3.3.1, the distance adds up as follows: from the focal spot to the tube exit (102 mm), from the tube exit to the PC (29 mm), the length of the collimator structure (160 mm) and the air gap (40 mm) and 10 mm WED, resulting in 341 mm SAD.

It is important to note, that measurements taken for a definition at the reference point were defined in 10 mm WED. This distance was defined by the SSD, which corresponded to the distance between the focal spot of the X-ray tube and the

surface of the phantom, which was 10 mm in front of the reference point. The SSD was set to 331 mm in μ-RayPhysics and added to the headers for the import of LDPs and DDPs.
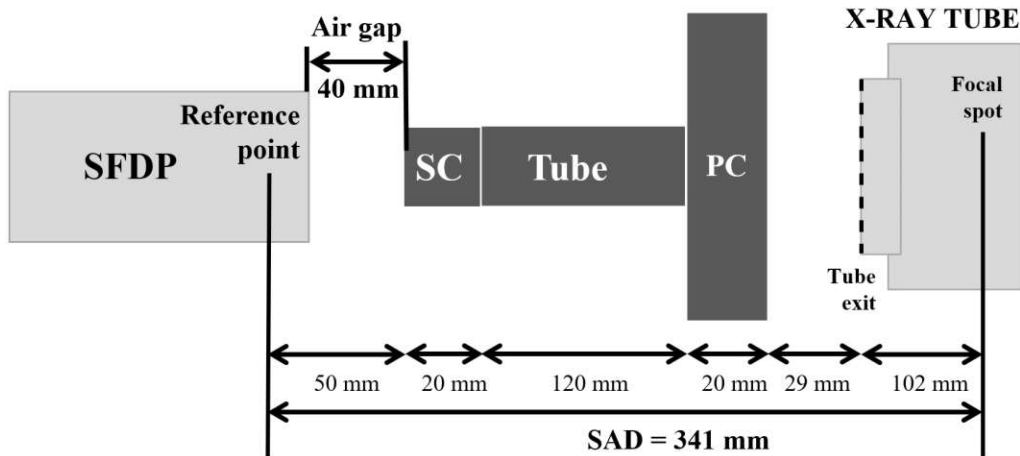

Abbildung 3.3.1: Schematic illustration of the SAD defined as the distance between the focal spot of the X-ray tube and the reference point.

Cones

For the collimators, in the μ-RayPhysics module called cones, the following characteristics were required: the collimator shape, the physical position and the X-width in centimeter. All collimators, PC and SCs, have a circular aperture. The physical position was defined as the distance from the focal spot of the X-ray tube to the start and the exit of the collimator. The PC was defined as the entrance collimator and the physical position was set to 151 mm. The SCs were defined as cones with their physical position of 271 mm to 291 mm, due to 20 mm thickness of the SCs. The X-width was defined as the field size measured at the reference point with Gafchromic^{TM} EBT3 films (Ashland Inc., Wayne, NJ, USA), as described in section 3.2.3.

Lateral Dose Profiles

The LDPs of the SCs at the reference point were measured for all eight SCs. To improve the accuracy of the beam model, it was recommended to import also LDPs along the beam path and not only at the reference point. Those LDPs were measured between 0 mm and 50 mm WED. The LDPs for the major collimator diameters were measured in intervals of 5 mm WED, resulting in 11 films for each SC with following diameters: 5 mm, 10 mm, 15 mm, 30 mm. For the remaining 4 collimators (diameters: 7 mm, 8 mm, 20 mm and 25 mm), LDPs were only measured in intervals of 10 mm WED, resulting in 6 films for each SC. In total

68 films were irradiated. The films were read vertical and horizontal and the dose values were normalised to the maximum. 136 LDPs were imported into µ-RayPhysics.

The widths of the LDPs at the reference point were defined as the field sizes of the SCs and were inserted in the cone definitions as X-widths.

Depth Dose Profiles

DDPs were measured with the microDiamond detector. The measurements were conducted with 40 mm air gap. The depth within the SFDP was adjusted by the number of inserted RW3 slabs, starting with 0 mm WED up to 50 mm WED in steps of 5 mm. The dose was calculated as mean values of three equivalent, consecutive measurements. The DDPs were measured for all 8 SCs and, as the LDPs, imported with headers. Additionally, µ-RayPhysics requires a reference curve measured for the reference field size. As reference field size the 8 mm aperture was chosen. The DDP for this SC was imported a second time as a reference curve, resulting in 9 DDPs imported into µ-RayPhysics.

3.3.2 µ-RayPlanning

After successful commissioning, treatment plans for validation measurements were created. First step was to create a virtual phantom in the patient modeling module of µ-RayStation. The phantom was defined large enough to contain the entire setup. It was positioned with 40 mm air gap to the beam exit and as material RW3 was assigned. For the calculation of the validation plans, 4 SCs were selected (5 mm, 8 mm, 15 mm and 30 mm diameter).
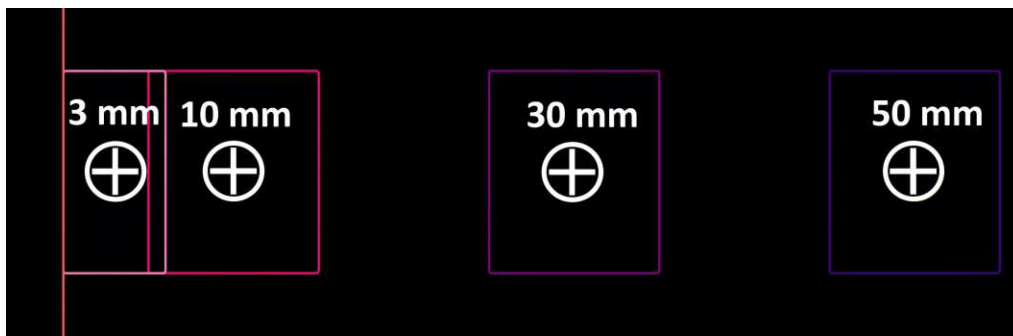

Abbildung 3.3.2: In the µ-RayPlanning module targets were created for the export of dose-time information. Shown are 4 targets, each with a diameter of 12 mm, positioned at 3 mm, 10 mm, 30 mm and 50 mm depths for the 15 mm aperture.

For each SC, 4 targets were created within the phantom, as shown in Figure 3.3.2 for the 15 mm aperture. RW3 was assigned as material to the targets and they were positioned in the phantom at the following depths: 3 mm, 10 mm, 30 mm and

50 mm. All targets had a length of 10 mm, except the 3 mm target which only had a length of 6 mm due to geometrical considerations. The targets were defined with a smaller diameter than the diameter of the corresponding SC, to ensure that the target is enclosed by the beam: 4 mm diameter for the 5 mm aperture, 6 mm diameter for the 8 mm aperture, 12 mm diameter for the 15 mm aperture and 25 mm diameter for the 30 mm aperture.

For each target, a treatment plan was created with prescribed median dose (50%). In total 24 treatment plans were created, as listed in section 4.2.1 in Table 4.3. For each SC, a treatment plan was prepared for each target isocenter with a prescribed dose of 200 cGy. For the 8 mm aperture, additionally treatment plans with 100 cGy and 500 cGy prescribed dose at the target isocenters were investigated. The different dose levels resulted in different treatment times. The TPS calculated the 3-dimensional dose distributions for each treatment plan and the required irradiation time for the X-ray unit to fulfil the prescription. A script, that automates dose calculation and data output, was developed. The script generates 3-dimensional dose grids, including the required irradiation time. In the following, the DDP along the central axis was extracted and saved along with the corresponding depths.

3.3.3 Beam Model Validation

As described in the previous section 3.3.2, the TPS calculated the dose distribution and the required irradiation time for the prescribed settings. For the validation measurements, the calculated irradiation time was set in the X-ray unit. The dosimetric measurements were done in the SFDP using the microDiamond detector. The deposited dose was measured at the isocenter of the target, in which the dose was prescribed, but also outside the targets in different depths.

4 Results

In the following sections, the results of the beam model creation and validation are presented. First, the results for the X-ray beam characterisation are described in section 4.1 including the X-ray spectrum, the lateral dose profiles (LDPs), the depth dose profiles (DDPs) and the irradiation time deviation of the X-ray unit. Next, the results of the beam model validation are shown and discussed in section 4.2.

4.1 X-ray Beam Characterisation

4.1.1 Source

In µ-RayStation, the source was defined by the tube current, the steady dose rate, the half rise time and the energy spectrum. The tube current was established at a constant 20 mA setting. A steady dose rate of 3.241 cGy/s was measured at the reference point for the reference field (SC with 8 mm diameter). The half rise time, defined as time to reach half the steady dose rate, was determined by the measurement of time-resolved dose. The half-rise time was observed to be negligible, compared to the expected irradiation time.
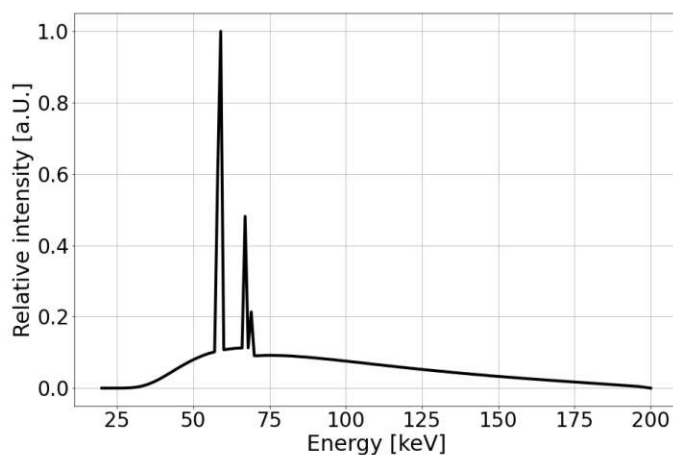

Abbildung 4.1.1: X-ray spectrum for a tungsten target, 20° target angle, 200 keV tube voltage, 20 mA current and 3.0 mm Be, 3.0 mm Al, 0.5 mm Cu inherent filtration calculated using SpekCalc [51].

4 Results

The energy spectrum was calculated using the software program SpekCalc, resulting in the spectrum shown in Figure 4.1.1. The used parameters include the peak energy, the target angle and the filters of the tube.

4.1.2 Lateral Dose Profiles

To determine the LDPs of the collimated photon beam, EBT3 films were irradiated. An example of an irradiated film is shown in Figure 4.1.2 (a). LDPs were obtained from irradiated films as described in section 3.2.3. Figure 4.1.2 (b) shows the crossline (horizontal) LDP for the 15 mm aperture in 5 mm WED.
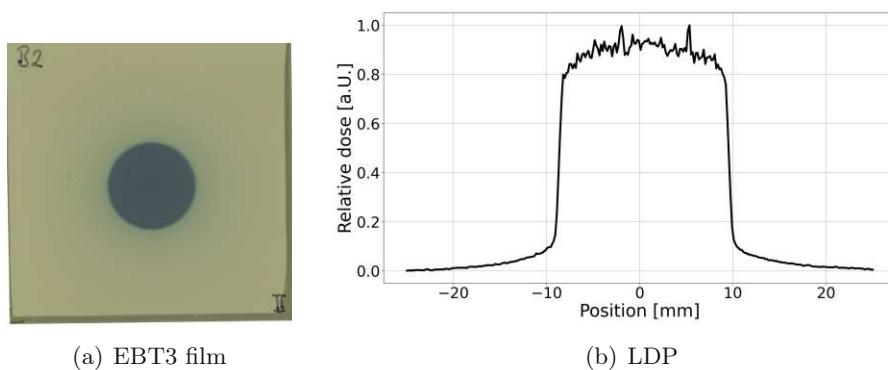

(a) EBT3 film   (b) LDP

Abbildung 4.1.2: (a) EBT3 film irradiated using 15 mm aperture in 5 mm WED
(b) crossline (horizontal) LDP for the 15 mm aperture in 5 mm WED.

For the definition of the SCs in µ-RayPhysics, the beam width was measured for the films at the reference point. It was defined as the width of the dose profile limited to 50% dose decay [32]. The resulting widths corresponded to the field sizes of the SCs and are listed in Table 4.1.

4.1.3 Depth Dose Profiles

The DDPs were measured in the SFDP using the microDiamond detector. As shown in Figure 4.1.3 for the SC with 8 mm diameter, the DDP, normalised to the maximum, showed an exponentially decreasing behaviour.

The DDPs were measured for all SCs and imported into µ-RayPhysics. Additionally, the beam model relies on a reference field for which a reference curve must be recorded. In our case, the SC with 8 mm diameter was chosen as collimator for the reference field. In the case of this particular SC, the DDP was imported twice, once as reference curve and once for the SC definition.

42

SC	Field size	
diameter	Inline [mm]	Crossline [mm]
5 mm	5.8	5.9
7 mm	8.3	8.5
8 mm	9.5	9.5
10 mm	11.9	11.9
15 mm	17.8	17.8
20 mm	23.7	24.1
25 mm	30.1	30.3
30 mm	35.6	36.1

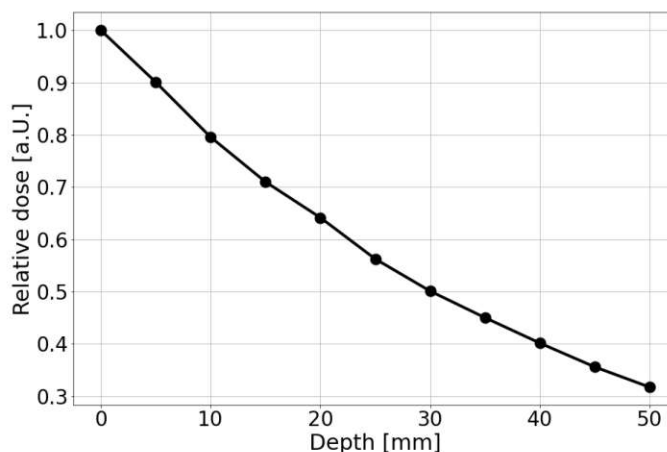Tabelle 4.1: Inline (vertical) and Crossline (horizontal) measured field size diameters for the SCs.

Abbildung 4.1.3: DDP of the 8 mm aperture, which was also imported as DDP for the reference field.

4.1.4 Time Deviation of the X-ray Unit

During measurements, it was found that the timing electronics of the X-ray unit showed instabilities. Repeated measurements yielded different results, up to 5% difference. To investigate the deviations in more detail, time-resolved dosimetric measurements were recorded with an in-house developed software. The dose was measured in 0.5 second intervals. In total 242 measurements with irradiation times between 28 seconds and 6 minutes 30 seconds were recorded and processed. By assuming a linear behavior between irradiation time and applied dose, the difference between nominal and calculated irradiation time was determined including standard deviation, as shown in Figure 4.1.4. The average of the total irradiation time was between −0.5 and +1.0 seconds. For evaluation

purposes, the deviations that were collected for all measurements were grouped as listed in Table 4.2. 113 values (46.7%) showed no deviation and the measurements corresponded to the specified time. 79.3% of the measurement deviations were in the range between -0.5 and $+0.5$ seconds. As the measurement could only be recorded with a time resolution of 0.5 seconds, deviations of $\pm$ 0.5 were expected. Irradiation time deviations above 1.5 seconds were excluded from the validation data and repeated if necessary.
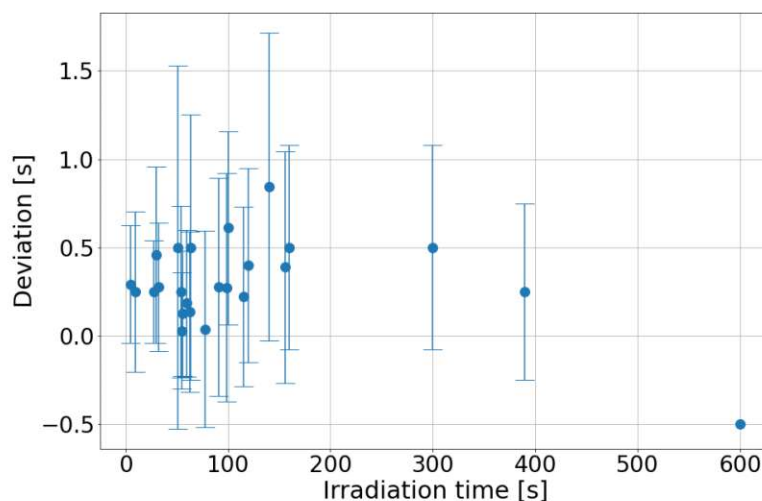
Abbildung 4.1.4: Time deviation with standard deviation per irradiation time.

Time deviation [s]	Number of measurements
−0.5	24 (9.9%)
0.0	113 (46.7%)
+0.5	55 (22.7%)
+1.0	35 (14.5%)
+1.5	10 (4.1%)
+2.0	3 (1.3%)
+3.0	2 (0.8%)

Tabelle 4.2: Time deviation steps in total number of measurements and percentage.

4.2 Beam Model Validation

As described in section 3.3.3, treatment plans for the validation measurements were created in the treatment planning module of the TPS. The validation plans had prescribed doses in the defined targets, which all had a length of 10 mm, except the 3 mm target which only had a length of 6 mm due to geometrical considerations. The treatment plans are listed in Table 4.3. The resulting dose distribution and the required irradiation time were calculated by the TPS.

In Figure 4.2.1 (a) the dose distribution and in Figure 4.2.1 (b) the corresponding DDP for the treatment plan D10 for the 15 mm aperture is shown. For this treatment plan, 200 cGy dose was prescribed at 10 mm WED from the surface of the SFDP, namely at the reference point which was defined in a distance of 50 mm from the SC exit.

Figure 4.2.2 shows the comparison of DDPs for the treatment plans D05, D06, D07 and D08. These were defined for the 8 mm aperture with 200 cGy prescribed dose to the targets, while the isocenters of these targets were located in depths of 3 mm, 10 mm, 30 mm and 50 mm. The dose was scaled to the median dose (50%) to the target structure. To deliver the identical dose to increasing depths in the SFDP, an increasing irradiation time was required, determined by the TPS. For the validation of the calculated dose distribution, the required irradiation time was set and the deposited dose was measured in the SFDP using the microDiamond detector. For the validation, the calculated and the measured dose were compared to each other.

4.2.1 Dose Validation at the Target Isocenter

Figure 4.2.3 (a-d) shows the dose distributions in the targets calculated by the TPS scaled to the prescription. Table 4.3 summarises all validation measurements with the corresponding deviations between measurements and dose prediction at the respective isocenter of each target. The dose values for the treatment plans D01-D04 defined for the 5 mm aperture in different depths showed lower measured dose values than predicted by the dose calculation. The deposited dose was overestimated by the TPS. The maximum deviation was -9.8% for the treatment plan D03 in 30 mm WED. This was also the maximum deviation for all measurements in the target isocenters. For the 8 mm aperture, the measured dose agreed well with the calculation. For the treatment plans with 200 cGy prescribed (D05-D08) as well as for the plans with 100 cGy and 500 cGy prescribed dose (D17, D18, D20, D21, D22 and D24) measurements were within tolerance levels. The maximum deviations for this aperture were reached with -1.7% for the treatment plan D06 in 10 mm WED and +1.7% for treatment plan D17 in 3 mm WED. For the larger SCs with 15 mm and 30 mm diameter, the dose was underestimated by the TPS. For the 15 mm aperture, a maximum deviation of +5.8% was achieved in treatment plan D12 in 50 mm WED. For the 30 mm aperture, the maximum of +8.1% was reached for the target isocenter in 3 mm WED (plan D13).
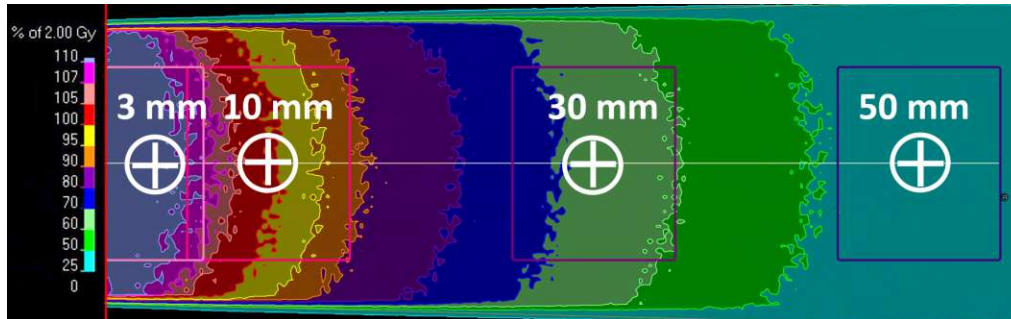
(a) Dose distribution
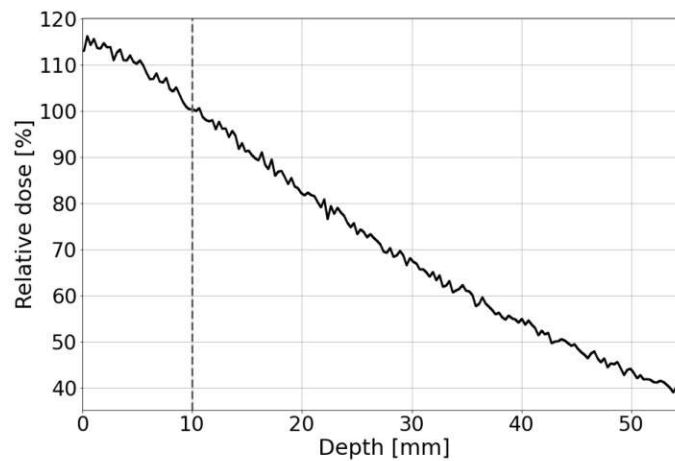
(b) Depth dose profile

Abbildung 4.2.1: (a) Dose distribution in the virtual phantom containing the targets (boxes) (b) Corresponding dose line calculated by the TPS for the treatment plan D10: 15 mm diameter aperture, 200 cGy prescribed dose in 10 mm WED. The dose line was extracted along the central axis and represents the calculated DDP without smoothing.

Plan ID	SC diameter	Prescribed dose [cGy]	Target isocenter position	Irr. time [s]	Relative deviation [%]
D01	05 mm	200	3 mm	55	−2.6
D02	05 mm	200	10 mm	63	−6.9
D03	05 mm	200	30 mm	99	−9.8
D04	05 mm	200	50 mm	156	−7.4
D05	08 mm	200	3 mm	56	+1.3
D06	08 mm	200	10 mm	64	−1.7
D07	08 mm	200	30 mm	100	−1.5
D08	08 mm	200	50 mm	156	−0.2
D09	15 mm	200	3 mm	54	+3.8
D10	15 mm	200	10 mm	60	+4.0
D11	15 mm	200	30 mm	91	+3.1
D12	15 mm	200	50 mm	140	+5.8
D13	30 mm	200	3 mm	51	+8.1
D14	30 mm	200	10 mm	55	+3.9
D15	30 mm	200	30 mm	78	+4.6
D16	30 mm	200	50 mm	115	+3.1
D17	08 mm	100	3 mm	28	+1.7
D18	08 mm	100	10 mm	32	−1.5
D20	08 mm	100	50 mm	78	−0.2
D21	08 mm	500	3 mm	140	+1.5
D22	08 mm	500	10 mm	160	−1.5
D24	08 mm	500	50 mm	390	−0.4

Tabelle 4.3: Results for the dose validation measurements in the target isocenters for 22 treatment plans. The target isocenter was related to the SSD with 40 mm air gap. The position at 10 mm depth thus corresponds to the reference point. The relative deviation refers to the calculated deposited dose in the target isocenter.
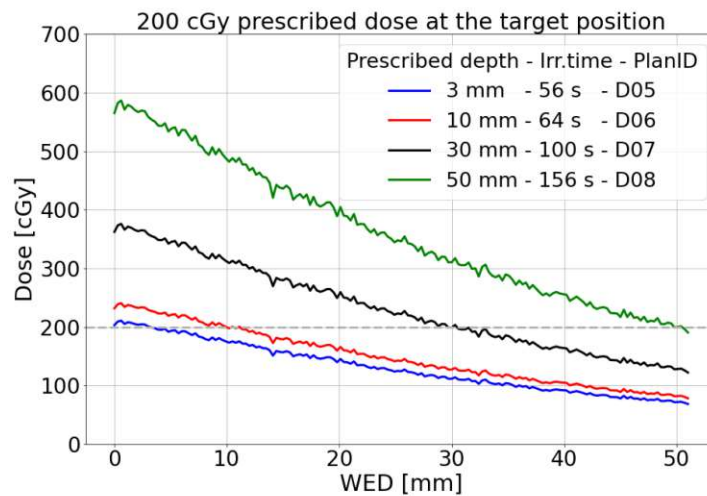
Abbildung 4.2.2: DDPs of the 8 mm aperture for the treatment plans D05, D06, D07 and D08 defined with 200 cGy prescribed dose in 3 mm, 10 mm, 30 mm and 50 mm WED. Data was not post-processed (smoothed) after TPS export to preserve data integrity and guarantee reproducibility.

4.2.2 Dose Validation outside the Target Region

As described in section 3.3.3, the deposited dose was measured in the isocenters of the target to which the dose was prescribed, but also outside the target in different depths. Therefore, the DDP along the central axis was extracted and the measured dose values were compared to the calculated ones.

In Figure 4.2.4 (a)-(d) the DDPs calculated by the TPS were compared with the measured dose values for the treatment plans D02, D06, D10 and D14. For all of these treatment plans, 200 cGy dose was prescribed to the target in 10 mm depth. Figure 4.2.4 (a) shows the treatment plan D02 for the 5 mm aperture. The experimentally determined dose values were -7.1 cGy to -13.6 cGy lower than predicted by the TPS. The maximum of -6.9% was measured in 11 mm WED. Figure 4.2.4 (b) shows the comparison for treatment plan D06 for the 8 mm aperture. The validation measurements agreed quite well with the calculated dose line. Dose deviations between -3.5 cGy and +3.0 cGy were measured. The maximum deviation was measured in 11 mm WED, corresponding to -1.7% deviation from the calculated dose. In Figure 4.2.4 (c) the treatment plan D10 for the 15 mm aperture is shown. The measurements lied above the calculated DDP and the dose was thus underestimated by the TPS. The measurements deviated between +3.4 cGy and +10.9 cGy. The maximum deviation +10.9 cGy was measured in 9 mm WED, corresponding to +5.4% deviation to the calculated dose value. The treatment plan D14 for the 30 mm aperture is shown in Figure
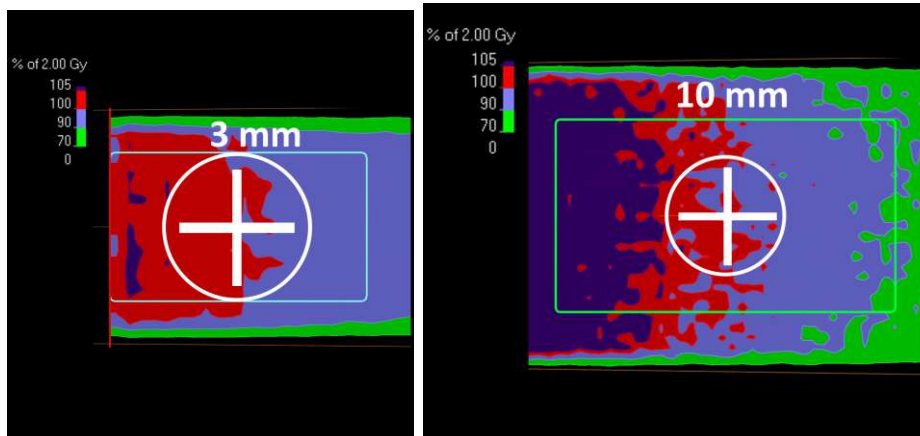
(a) 5 mm aperture - Plan D01

(b) 8 mm aperture - Plan D06
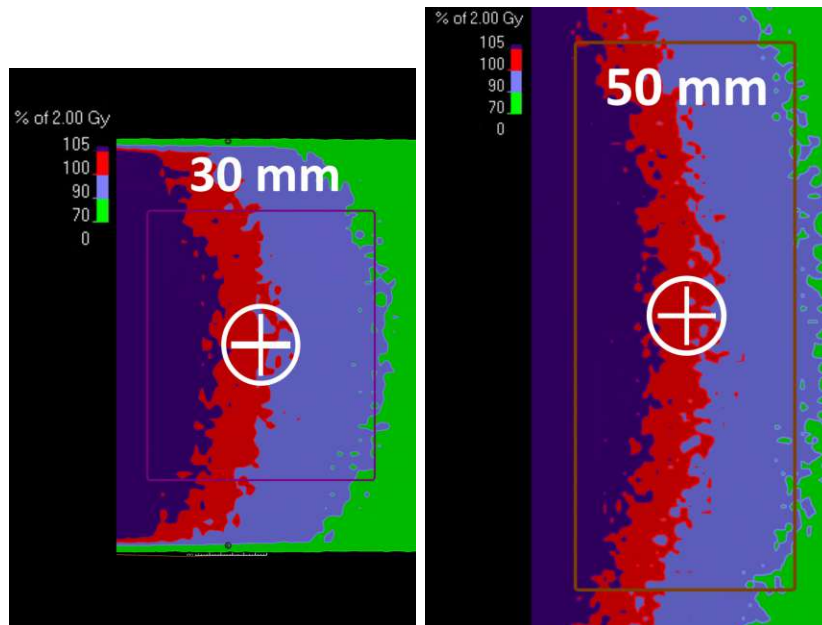
(c) 15 mm aperture - Plan D11

(d) 30 mm aperture - Plan D16

Abbildung 4.2.3: Dose distributions shown in the targets (boxes) calculated by the TPS for 200 cGy prescribed dose. The beam direction was from left to right.
(a) treatment plan D01 - 5 mm aperture, target isocenter in 3 mm WED (b) treatment plan D06 - 8 mm aperture, target isocenter in 10 mm WED (c) treatment plan D11 - 15 mm aperture, target isocenter in 30 mm WED (d) treatment plan D16 - 30 mm aperture, target isocenter in 50 mm WED.

(a) 5 mm aperture - Plan D02

(b) 8 mm aperture - Plan D06

(c) 15 mm aperture - Plan D10
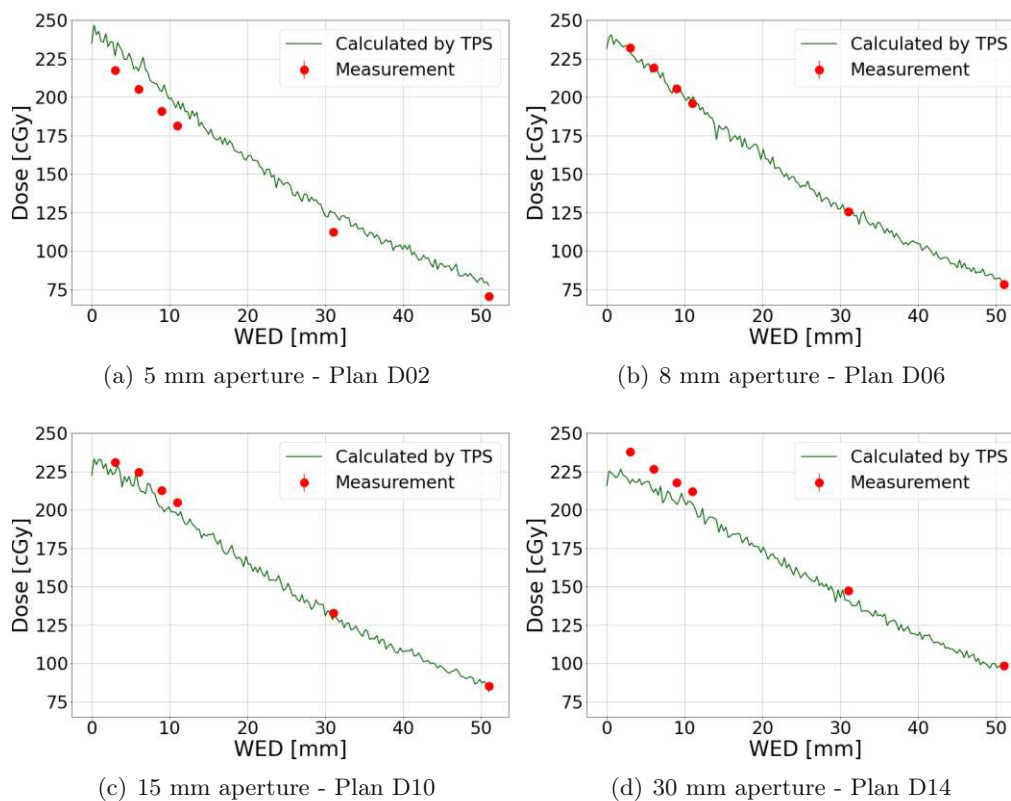
(d) 30 mm aperture - Plan D14

Abbildung 4.2.4: Comparison of calculated DDPs by the TPS and measured dose values. The treatment plans were scaled to 200 cGy prescribed dose in 10 mm WED (a) treatment plan D02 for the 5 mm aperture (b) treatment plan D06 for the 8 mm aperture (c) treatment plan D10 for the 15 mm aperture (d) treatment plan D14 for the 30 mm aperture.
The error bars in the graph are not visible due to their relatively small size in comparison to the marker used to visualise the data point.

4.2.4 (d). The dose for this SC was also underestimated. Especially for the value closest to the surface in 3 mm WED, a deviation of +19.2 cGy was measured. The deviation corresponds to +8.8% of the calculated dose value.

In Figure 4.2.5 the relative dose deviation related to the calculated values for the treatment plans D01-D16 are shown. The treatment plans were defined with a prescribed dose of 200 cGy. The deviations from the prescribed dose were compared in different WEDs (3 mm, 11 mm, 31 mm, 51 mm). Figure 4.2.5 (a) shows the relative deviation for the 5 mm aperture. The deviations in dose were measured between -2.6% and -10.2%. The maximum deviation was observed for the treatment plan D04 in 31 mm WED. In Figure 4.2.5 (b) the relative deviation for the 8 mm aperture is shown. The measurements agreed well with the calculated dose values. The deviations were between -1.9% and +1.7%. The maximum deviation of -1.9% was measured for the treatment plan D05 in 11 mm WED. For the larger SCs with 15 mm and 30 mm diameter, the dose was underestimated by the TPS. The measured dose values were 2.6% to 8.8% higher than predicted. For the 15 mm aperture, the maximum deviation of +5.9% was reached for the treatment plan D12 in 3 mm WED. For the 30 mm aperture, the maximum deviation of +8.8% was measured for the treatment plan D14 in 3 mm WED, as already shown in 4.2.4 (d).

In Figure 4.2.6 the relative deviations for the treatment plans with 100 cGy and 500 cGy prescribed dose are shown (D17, D18, D20, D21, D22 and D24). These treatment plans were all created for the 8 mm aperture. For the treatment plans D17, D20, D21 and D24, the dose was measured in 3 mm and 51 mm WED. For D18 and D22, additionally 11 mm and 31 mm WED were measured. The measured deviations behave very similarly. The maximum deviations were reached with -1.5% for the treatment plans D18 and D22.

WED [mm]	Relative deviation	
	mean [%]	std [%]
3.0	+2.2	4.0
6.0	+1.4	5.5
9.0	+1.9	5.8
11.0	−0.1	4.6
31.0	−0.7	5.4
51.0	+0.1	4.3

Tabelle 4.4: Relative deviations for the measured WEDs. The mean deviation was calculated by averaging the relative deviation of the measured dose.

In Table 4.4 mean and the standard deviation for the relative deviations in different WEDs are given. The table shows that the measurements in 3 mm WED had the highest mean deviation of +2.2%. The dose values in 11 mm WED and 51 mm WED agreed the best with ±0.1% mean deviation.

(a) 5 mm aperture

(b) 8 mm aperture

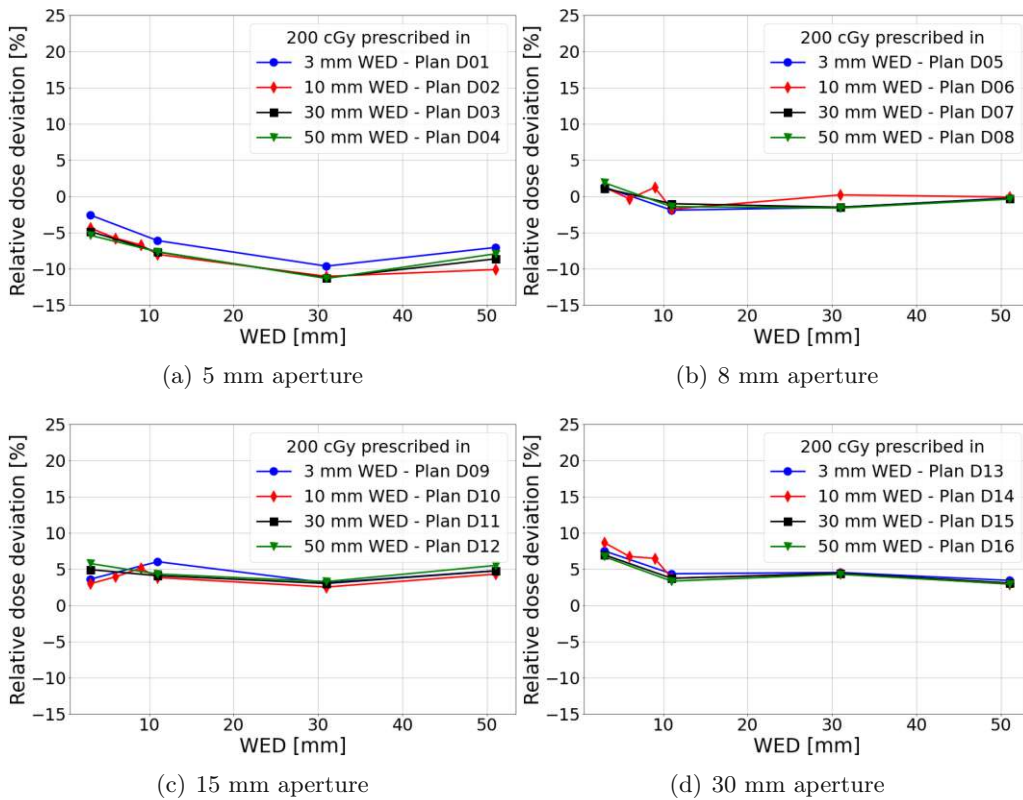(c) 15 mm aperture

(d) 30 mm aperture

Abbildung 4.2.5: Relative dose deviations for (a) treatment plans D01-D04 for the 5 mm aperture (b) treatment plans D05-D08 for the 8 mm aperture (c) treatment plans D09-D12 for the 15 mm aperture (d) treatment plans D13-D16 for the 30 mm aperture.
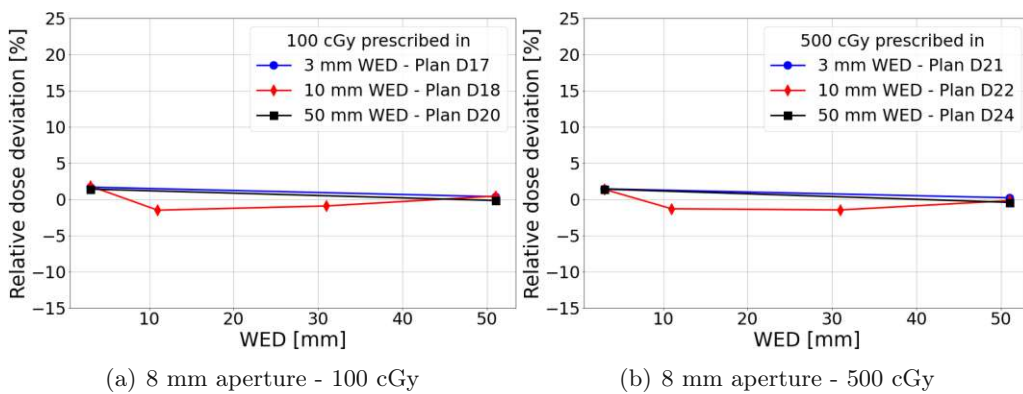

(a) 8 mm aperture - 100 cGy

(b) 8 mm aperture - 500 cGy

Abbildung 4.2.6: Relative dose deviations for (a) treatment plan D17, D18, D20 - 8 mm aperture (b) treatment plan D21, D12, D24 - 8 mm aperture.

5 Discussion and Outlook

In this thesis, a beam model for an X-ray unit for pre-clinical research was created and validated for the TPS µ-RayStation 8B (RaySearch Laboratories, Stockholm, Sweden). In the upcoming pre-clinical studies, this X-ray setup will act as reference system for the comparison with particle beam irradiation. The beam model was created utilising a small animal irradiation setup consisting of an in-house developed, non commercial beam collimation system, a positioning table with a couch and a SFDP for dosimetric measurements. After the definition of the irradiation geometry, measurements for the characterisation of the X-ray beam were conducted. The characterisation of the collimated photon beam was crucial for the accuracy of the model. DDPs and LDPs were measured using the SFDP. Field sizes and dose rates were determined at the reference point. The measured data was imported into the µ-RayPhysics module of the TPS. After the commissioning of the beam model, the geometry for validation measurements was created in the treatment planning module. Dedicated treatment plans for the validation were generated. The dose distribution and the required irradiation time for the photon beam were calculated by the TPS. To validate the beam model the calculated DDP was compared to the deposited dose measured in the SFDP with the microDiamond detector. Dose measurements were taken in all target isocenters and in defined depths.

The reference SC (8 mm) exhibited deviations of less than 2%. Overall, the validation for the 8 mm aperture achieved the best result. This was mainly due to the fact that the DDP for this aperture was imported as reference profile and the other SCs were derived from it. On the other hand, this collimator was less sensitive to positioning inaccuracies than the smaller apertures, where the beam path was slightly affected by instabilities. For the smaller SC (5 mm), the deviation reached up to -10.2% in 31 mm WED. The larger deviation for the smallest field size underlined the requirements of accurate positioning. However, the currently used positioning table is limited in its stability, resulting in a decreased level of accuracy. Improving the table will be a next step to enhance precision and reliability. The larger apertures (15 mm and 30 mm) exhibited maxima of +5.9% and +8.8% respectively. However, both maxima were measured in close proximity to the surface. By comparing the measurement deviations per depth, the measurements in 3 mm WED had the highest mean deviation of +2.2%.

Similar results were reported for the validation of the treatment planning platform SmART-Plan [60]. The calculated depth dose curves and dose distributions were also determined using Monte Carlo calculations. Results within 5% for the 5 mm and 15 mm circular collimators were presented. In comparison to van Hoof et al,

in our study slightly higher deviations were measured: 6% for the 15 mm and 10% for the 5 mm aperture. Furthermore, it was described that the smallest collimator also had the largest deviation [60].

In [61] the orthovoltage unit Xstrahl 300 (Xstrahl Ltd., Surrey, UK) was used, which is comparable to the YXLON X-ray unit used in our study. The Xstrahl unit delivers kilovoltage X-ray beams of 40–300 kVp for superficial treatments and is not initially equipped with distance indicator or crosshair projection. The development of a chamber positioning system, a mechanical distance pointer and a crosshair projector was reported by Lim et al [61]. An accuracy of 0.1 mm was achieved for the positioning of the dosimeters. A similar alignment system was also recently installed in the YXLON X-ray cabinet used in our study. However, for the measurements performed in our study the setup was still aligned manually. It is estimated that the accuracy of the positioning was between 2 mm and 3 mm. The alignment system is expected to improve positioning and thus reduce the uncertainties of future measurements. Since the visual beam of the laser alignment system has a width of 1 mm, this value serves as a lower limit for the system's ability to accurately position objects. Commercial irradiation systems offer an accuracy of under 1 mm. The small animal radiation research platform (SARRP) (Xstrahl Ltd., Camberley, UK) system, for example, provides an accuracy of 0.2 mm with a positioning system using a rotating stage [62, 63]. In comparison to the SARRP the used X-ray setup is less complex. Since the setup's primary aim is to act as reference irradiation system to a horizontal ion beam line, rotating elements were not required. SARRP is an image-guided radiotherapy system consisting of a micro irradiator, cone beam CT imaging, and a TPS [62, 64]. The TPS of the SARRP system sends the calculated dose with accompanying parameters to the irradiator for treatment delivery. Such automated workflow is not provided in our system and imaging, TPS and dose delivery are independent processes. In addition, the time setting system of the X-ray unit can only be set manually.

Another limitation of this study was the observed time deviation of the X-ray unit (section 4.1.4). It was shown that the time setting deviates. The reason for the time deviation is not yet fully understood, whether they are caused by the external time control unit of the X-ray irradiator or by the tube properties. Further investigations are required to determine the reasons and implications of these deviations.

For commercial systems, the vendors offer beam collimation down to 0.5 mm diameter field size [65]. In our current range of apertures, the 5 mm aperture offers the narrowest beam collimation. With this beam size, the setup had to be positioned as precisely as possible, otherwise the beam path would deviate too much for dose measurements using the microDiamond detector.

A steady dose rate of 3.2 cGy/s (1.9 Gy/min) was measured at the reference point for the reference field size (8 mm aperture). For commercial systems, the dose rate is in the region of 1–3 Gy/min [6, 63, 66]. Therefore with the developed small animal irradiation system, dose rates can be achieved that are comparable

to those of commercially available systems.

A gamma index analysis would have potential benefits understanding the behaviour of the dose calculation in comparison to e.g. film measurements, like performed by Entezam et al [67]. Such analysis provides a quantitative comparison between the calculated and measured dose profiles by creating an acceptance region in the calculated dose distribution. A gamma index analysis was not performed in the scope of this thesis due to constraints on time and resources.

The currently used beam collimation system consisted of the PC and eight exchangeable SCs with diameters between 5 mm and 30 mm. In future research with small animals, the range of apertures may be extended if more intermediate sizes are needed.

After the improvements, some of the measurements will be repeated to determine if any improvements occurred. Afterwards, the beam model in the TPS might be adapted and the dose-time information recalculated.

A comprehensive end-to-end test is currently prepared and designed, but this is beyond the scope of this project. In an end-to-end test, the entire process of imaging, planning and irradiation will be checked. To ensure precise and reliable irradiation, the entire process must be tested using the appropriate detectors and phantoms. Completion of the final technical modifications and end-to-end testing are necessary prerequisites before commencing the first pre-clinical irradiation.

For irradiation with protons, a next step will be to create a beam model in the respective research treatment planning system. The irradiation with carbon ions is foreseen after completing all task for pre-clinical animal research with proton beams, and is currently planned for 2024.

Abbildungsverzeichnis

Literatur

[1]   WHO. *World Health Organization*. URL: https://www.who.int/news-room/fact-sheets/detail/cancer (besucht am 12.01.2023).

[2]   IARC. *IARC CancerToday*. URL: https://gco.iarc.fr/today/home (besucht am 12.01.2023).

[3]   S. Martinez-Pacheco und L. O'Driscoll. »Pre-clinical in vitro models used in cancer research: Results of a worldwide survey«. In: *Cancers (Basel)* 13.23 (2021), S. 6033. DOI: 10.3390/cancers13236033.

[4]   D. W. Hutmacher. »Biomaterials offer cancer research the third dimension«. In: *Nature materials* 9.2 (2010), S. 90–93. DOI: 10.1038/nmat2619.

[5]   C. Jubelin, J. Muñoz-Garcia, L. Griscom, D. Cochonneau, E. Ollivier, M.-F. Heymann, F. M. Vallette, L. Oliver und D. Heymann. »Three-dimensional in vitro culture models in oncology research«. In: *Cell & Bioscience* 12.1 (2022). DOI: 10.1186/s13578-022-00887-3.

[6]   F. Tillner, P. Thute, R. Bütof, M. Krause und W. Enghardt. »Pre-clinical research in small animals using radiotherapy technology – a bidirectional translational approach«. In: *Zeitschrift für medizinische Physik* 24.4 (2014), S. 335–351. DOI: 10.1016/j.zemedi.2014.07.004.

[7]   A. Anvari, A. Modiri, R. Pandita, J. Mahmood und A. Sawant. »Online dose delivery verification in small animal image-guided radiotherapy«. In: 47.4 (2020), S. 1871–1879. DOI: 10.1002/mp.14070.

[8]   K. H. Song, R. Pidikiti, S. Stojadinovic, M. Speiser, S. Seliounine, D. Saha und T. D. Solberg. »An x-ray image guidance system for small animal stereotactic irradiation«. In: *Physics in medicine & biology* 55.23 (2010), S. 7345–7362. DOI: 10.1088/0031-9155/55/23/011.

[9]   R. Schöfbeck. »Couch and Table Design for High-Precision x-Ray Irradiations«. Project Thesis. Vienna University of Technology, 2021.

[10] L. Langgartner. »Design and dosimetric validation of an irradiation setup for preclinical research with x-rays and protons«. Master Thesis. Wien: Vienna University of Technology, 2022.

[11] W. C. Röntgen. *Eine neue Art von Strahlen = Über eine neue Art von Strahlen*. 2. Aufl. Würzburg: Stahel, 1896.

[12] T. Pawlicki, D. J. Scanderbeg und G. Starkschall. *Hendee's radiation therapy physics*. 4th ed. Hoboken, New Jersey: Wiley Blackwell, 2016.

Literatur

[13] F. Khan. *The Physics of Radiation Therapy*. Sans tache. Williams & Wilkins, 1984.

[14] V. I. Mikla und V. V. Mikla. *Medical imaging technology*. Elsevier insights Medical imaging technology. London: Academic Press, 2014.

[15] R. P. Johnson. »Review of medical radiography and tomography with proton beams«. In: 81.1 (2018), S. 016701–016701. DOI: `10.1088/1361-6633/aa8b1d`.

[16] F. Vernimmen und K. Rock. »Technological Progress in Radiation Therapy for Brain Tumors«. In: *Journal of Cancer Therapy* 05 (Jan. 2014), S. 38–43. DOI: `10.4236/jct.2014.51005`.

[17] U. Linz. *Ion Beam Therapy - Fundamentals, Technology, Clinical Applications*. Berlin Heidelberg: Springer Science & Business Media, 2011.

[18] M. Jermann. *Particle Therapy Patient Statistics (per end of 2021)*. 2022. URL: `https://www.ptcog.ch/index.php/ptcog-patient-statistics` (besucht am 24.03.2023).

[19] H. Paganetti. »Relative biological effectiveness (RBE) values for proton beam therapy. Variations as a function of biological endpoint, dose, and linear energy transfer«. In: *Physics in Medicine & Biology* 59.22 (Okt. 2014), R419. DOI: `10.1088/0031-9155/59/22/R419`.

[20] H. Paganetti, E. Blakely, A. Carabe-Fernandez, D. J. Carlson, I. J. Das, L. Dong, D. Grosshans, K. D. Held, R. Mohan, V. Moiseenko und et al. »Report of the AAPM TG-256 on the relative biological effectiveness of proton beams in radiation therapy«. In: *Medical physics* (März 2019). DOI: `10.1002/mp.13390`.

[21] J. Gueulette, J. P. Slabbert, L. Böhm, B. M. De Coster, J.-F. Rosier, M. Octave-Prignot, A. Ruifrok, A. Nicolaas Schreuder, A. Wambersie, P. Scalliet und D. Jones. »Proton RBE for early intestinal tolerance in mice after fractionated irradiation«. In: *Radiotherapy and oncology* 61.2 (2001), S. 177–184. DOI: `10.1016/S0167-8140(01)00446-7`.

[22] C.-P. Segeritz und L. Vallier. »Chapter 9 - Cell Culture: Growing Cells as Model Systems In Vitro«. In: *Basic Science Methods for Clinical Researchers*. Hrsg. von M. Jalali, F. Y. Saldanha und M. Jalali. Boston: Academic Press, 2017, S. 151–172. DOI: `https://doi.org/10.1016/B978-0-12-803077-6.00009-6`.

[23] F. Verhaegen, P. Granton und E. Tryggestad. »Small animal radiotherapy research platforms«. In: *Physics in medicine & biology* 56.12 (2011), R55–R83. DOI: `10.1088/0031-9155/56/12/R01`.

[24] THE EUROPEAN PARLIAMENT AND THE COUNCIL OF THE EUROPEAN UNION. »DIRECTIVE 2010/63/EU OF THE EUROPEAN PARLIAMENT AND OF THE COUNCIL of 22 September 2010 on the protection of animals used for scientific purposes«. In: *Official Journal of the European Union* L 276/33 (2019).

[25] THE COMMISSION OF THE EUROPEAN COMMUNITIES. »COMMISSION RECOMMENDATION of 18 June 2007 on guidelines for the accommodation and care of animals used for experimental and other scientific purposes«. In: *Official Journal of the European Union* L 197/1 (2007).

[26] C. P. Karger und P. Peschke. »RBE and related modeling in carbon-ion therapy«. In: *PMB* 63.1 (Dez. 2017), 01TR02. DOI: 10.1088/1361-6560/aa9102.

[27] T. Suckert, J. Müller, E. Beyreuther, B. Azadegan, A. Brüggemann, R. Bütof, A. Dietrich, M. Gotz, R. Haase, M. Schürer, F. Tillner, C. von Neubeck, M. Krause und A. Lühr. »High-precision image-guided proton irradiation of mouse brain sub-volumes«. In: *Radiother Oncol* 146 (Mai 2020), S. 205–212. DOI: 10.1016/j.radonc.2020.02.023.

[28] F. Tillner, P. Thute, S. Löck, A. Dietrich, A. Fursov, R. Haase, M. Lukas, B. Rimarzig, M. Sobiella, M. Krause, M. Baumann, R. Bütof und W. Enghardt. »Precise image-guided irradiation of small animals: a flexible non-profit platform«. In: *Physics in medicine & biology* 61.8 (2016), S. 3084–3108. DOI: 10.1088/0031-9155/61/8/3084.

[29] S. Chiavassa, R. Nilsson, K. Clément-Colmou, V. Potiron, G. Delpon und E. Traneus. »Validation of the analytical irradiator model and Monte Carlo dose engine in the small animal irradiation treatment planning system μ-RayStation 8B«. In: *Physics in medicine & biology* 65.3 (2020), S. 035006–035006. DOI: 10.1088/1361-6560/ab6155.

[30] P. Kuess, E. Bozsaky, J. Hopfgartner, G. Seifritz, W. Dörr und D. Georg. »Dosimetric challenges of small animal irradiation with a commercial X-ray unit«. In: *Zeitschrift für Medizinische Physik* 24.4 (2014). Schwerpunkt: Medizinphysik in der prä-klinischen Forschung, S. 363–372. DOI: 10.1016/j.zemedi.2014.08.005.

[31] U. Schneider, E. Pedroni und A. Lomax. »The calibration of CT Hounsfield units for radiotherapy treatment planning«. In: *Physics in medicine & biology* 41.1 (1996), S. 111–124. DOI: 10.1088/0031-9155/41/1/009.

[32] P. Mayles. *Handbook of radiotherapy physics : theory and practice*. New York, NY [u.a.]: Taylor & Francis, 2007.

[33] W. D. Newhauser und R. Zhang. »The physics of proton therapy«. In: 60.8 (2015), R155–R209. DOI: 10.1088/0031-9155/60/8/R155.

Literatur

[34] E. B. Podgorsak. *Radiation physics for medical physicists : with 80 tables.* 2., enl. ed. Biological and medical physics, biomedical engineering. Berlin [u.a.]: Springer, 2010.

[35] G. Poludniowski, N. M. Allinson und P. M. Evans. »Proton radiography and tomography with application to proton therapy«. In: *British journal of radiology* 88.1053 (2015), S. 20150134–20150134. DOI: `10.1259/bjr.20150134`.

[36] S. Jan, D. Benoit, E. Becheva, T. Carlier, F. Cassol, P. Descourt, T. Frisson, L. Grevillot, L. Guigues, L. Maigne, C. Morel, Y. Perrot, N. Rehfeld, D. Sarrut, D. R. Schaart, S. Stute, U. Pietrzyk, D. Visvikis, N. Zahra und I. Buvat. »GATE V6: a major enhancement of the GATE simulation platform enabling modelling of CT and radiotherapy«. In: *Physics in medicine & biology* 56.4 (2011), S. 881–901. DOI: `10.1088/0031-9155/56/4/001`.

[37] M. Bucciantonio und F. Sauli. »Proton computed tomography«. In: *Modern Physics Letters A* 30.17 (2015). DOI: `10.1142/S0217732315400246`.

[38] A. Darafsheh. *Radiation Therapy Dosimetry: A Practical Handbook.* CRC Press, 2021. DOI: `10.1201/9781351005388`.

[39] J. Osorio, R. Dreindl, L. Grevillot, V. Letellier, P. Kuess, A. Carlino, A. Elia, M. Stock, S. Vatnitsky und H. Palmans. »Beam monitor calibration of a synchrotron-based scanned light-ion beam delivery system«. In: *Zeitschrift für medizinische Physik* 31.2 (2021), S. 154–165. DOI: `10.1016/j.zemedi.2020.06.005`.

[40] *Absorbed Dose Determination in External Beam Radiotherapy.* Technical Reports Series 398. Vienna: INTERNATIONAL ATOMIC ENERGY AGENCY, 2001.

[41] G. F. Knoll. *Radiation detection and measurement.* 2. ed.. New York, NY [u.a.]: Wiley, 1989.

[42] J. A. Meli. *Physics of Radiation Dosimetry, The.* Melville, New York: AIP Publishing, 2020. DOI: `10.1063/9780735421882`.

[43] L. Grevillot, M. Stock, H. Palmans, J. Osorio Moreno, V. Letellier, R. Dreindl, A. Elia, H. Fuchs, A. Carlino und S. Vatnitsky. »Implementation of dosimetry equipment and phantoms at the MedAustron light ion beam therapy facility«. In: *Medical physics (Lancaster)* 45.1 (2018), S. 352–369. DOI: `10.1002/mp.12653`.

[44] »Reporting and analyzing statistical uncertainties in Monte Carlo–based treatment planning«. In: *International Journal of Radiation Oncology*Biology*Physics* 65.4 (2006), S. 1249–1259. DOI: `10.1016/j.ijrobp.2006.03.039`.

[45] J. V. Siebers, P. J. Keall, A. E. Nahum und R. Mohan. »Converting absorbed dose to medium to absorbed dose to water for Monte Carlo based photon beam dose calculations«. In: *Physics in medicine & biology* 45.4 (2000), S. 983–995. DOI: `10.1088/0031-9155/45/4/313`.

[46] H. Paganetti. »Dose to water versus dose to medium in proton beam therapy«. In: *Physics in medicine & biology* 54.14 (2009), S. 4399–4421. DOI: `10.1088/0031-9155/54/14/004`.

[47] P. Arce, J. I. Lagares, J. D. Azcona und P.-B. Aguilar-Redondo. »A proposal for a Geant4 physics list for radiotherapy optimized in physics performance and CPU time«. In: *Nuclear Instruments and Methods in Physics Research Section A: Accelerators, Spectrometers, Detectors and Associated Equipment* 964 (2020), S. 163755. DOI: `10.1016/j.nima.2020.163755`.

[48] S. Agostinelli u. a. »Geant4—a simulation toolkit«. In: *Nuclear Instruments and Methods in Physics Research Section A: Accelerators, Spectrometers, Detectors and Associated Equipment* 506.3 (2003), S. 250–303. DOI: `10.1016/S0168-9002(03)01368-8`.

[49] D. Sarrut, M. Bardiès, N. Boussion, N. Freud, S. Jan, J.-M. Létang, G. Loudos, L. Maigne, S. Marcatili, T. Mauxion, P. Papadimitroulas, Y. Perrot, U. Pietrzyk, C. Robert, D. R. Schaart, D. Visvikis und I. Buvat. »A review of the use and potential of the GATE Monte Carlo simulation code for radiation therapy and dosimetry applications«. In: *Medical physics (Lancaster)* 41.6 (2014), 064301–n/a. DOI: `10.1118/1.4871617`.

[50] M. Stock, D. Georg, A. Ableitinger, A. Zechner, A. Utz, M. Mumot, G. Kragl, J. Hopfgartner, J. Gora, T. Böhlen, L. Grevillot, P. Kuess, P. Steininger, H. Deutschmann und S. Vatnitsky. »The technological basis for adaptive ion beam therapy at MedAustron: Status and outlook«. In: *Zeitschrift für Medizinische Physik* 28.3 (2018), S. 196–210. DOI: `10.1016/j.zemedi.2017.09.007`.

[51] G. G. Poludniowski und P. M. Evans. »Calculation of x-ray spectra emerging from an x-ray tube. Part I. Electron penetration characteristics in x-ray targets«. In: *Medical Physics* 34.6Part1 (2007), S. 2164–2174. DOI: `10.1118/1.2734725`.

[52] R. Hill, Z. Kuncic und C. Baldock. »The water equivalence of solid phantoms for low energy photon beams: Water equivalence of phantoms for low energy photons«. In: *Medical physics (Lancaster)* 37.8 (2010), S. 4355–4363. DOI: `10.1118/1.3462558`.

[53] A. Inc. *Gafchromic dosimetry media, type EBT-3.* URL: `http://www.gafchromic.com/documents/EBT3_Specifications.pdf` (besucht am 29.04.2023).

[54] A. Niroomand-Rad, S.-T. Chiu-Tsao, M. P. Grams, D. F. Lewis, C. G. Soares, L. J. Van Battum, I. J. Das, S. Trichter, M. W. Kissick, G. Massillon-JL, P. E. Alvarez und M. F. Chan. »Report of AAPM Task Group 235 Radiochromic Film Dosimetry: An Update to TG-55«. In: *Medical Physics* 47.12 (2020), S. 5986–6025. DOI: `10.1002/mp.14497`.

[55] G. Van Rossum und F. L. Drake. *Python 3 Reference Manual.* Scotts Valley, CA: CreateSpace, 2009.

[56] S. Khachonkham, R. Dreindl, G. Heilemann, W. Lechner, H. Fuchs, H. Palmans, D. Georg und P. Kuess. »Characteristic of EBT-XD and EBT3 radiochromic film dosimetry for photon and proton beams«. In: *Physics in medicine & biology* 63.6 (2018), S. 065007–065007. DOI: `10.1088/1361-6560/aab1ee`.

[57] S. Devic, J. Seuntjens, E. Sham, E. B. Podgorsak, C. R. Schmidtlein, A. S. Kirov und C. G. Soares. »Precise radiochromic film dosimetry using a flat-bed document scanner«. In: *Medical Physics* 32.7Part1 (2005), S. 2245–2253. DOI: `10.1118/1.1929253`.

[58] R. Dreindl, D. Georg und M. Stock. »Radiochromic film dosimetry: Considerations on precision and accuracy for EBT2 and EBT3 type films«. In: *Zeitschrift für medizinische Physik* 24.2 (2014), S. 153–163. DOI: `10.1016/j.zemedi.2013.08.002`.

[59] PTW-Freiburg. »User Manual microDiamond Type 60019«. In: (2013).

[60] S. J. van Hoof, P. V. Granton und F. Verhaegen. »Development and validation of a treatment planning system for small animal radiotherapy: SmART-Plan«. In: *Radiotherapy and oncology* 109.3 (2013), S. 361–366. DOI: `10.1016/j.radonc.2013.10.003`.

[61] T. Y. Lim, D. Mirkovic, X. Wang und R. Tailor. »Devices for dosimetric measurements and quality assurance of the Xstrahl 300 orthovoltage unit«. In: *Journal of applied clinical medical physics* 22.4 (2021), S. 151–157. DOI: `10.1002/acm2.13220`.

[62] M. Jermoumi, H. Korideck, M. Bhagwat, P. Zygmanski, G. Makrigiogos, R. Berbeco, R. Cormack und W. Ngwa. »Comprehensive quality assurance phantom for the small animal radiation research platform (SARRP)«. In: *Physica medica* 31.5 (2015), S. 529–535. DOI: `10.1016/j.ejmp.2015.04.010`.

[63] S. Kampfer, M. A. Duda, S. Dobiasch, S. E. Combs und J. J. Wilkens. »A comprehensive and efficient quality assurance program for an image-guided small animal irradiation system«. In: *Zeitschrift für medizinische Physik* 32.3 (2022), S. 261–272. DOI: `10.1016/j.zemedi.2022.02.004`.

[64]   M. Matinfar, E. Ford, I. Iordachita, J. Wong und P. Kazanzides. »Image-guided small animal radiation research platform: calibration of treatment beam alignment«. In: *Physics in Medicine & Biology* 54.4 (2009), S. 891. DOI: 10.1088/0031-9155/54/4/005.

[65]   F. Verhaegen, K. T. Butterworth, A. J. Chalmers, R. P. Coppes, D. de Ruysscher, S. Dobiasch, J. D. Fenwick, P. V. Granton, S. H. J. Heijmans, M. A. Hill, C. Koumenis, K. Lauber, B. Marples, K. Parodi, L. C. G. G. Persoon, N. Staut, A. Subiel, R. D. W. Vaes, S. van Hoof, I. L. Verginadis, J. J. Wilkens, K. J. Williams, G. D. Wilson und L. J. Dubois. »Roadmap for precision preclinical x-ray radiation studies«. In: *Physics in medicine & biology* 68.6 (2023). DOI: 10.1088/1361-6560/acaf45.

[66]   M. Ghita, S. J. McMahon, H. F. Thompson, C. K. McGarry, R. King, S. O. S. Osman, J. L. Kane, A. Tulk, G. Schettino, K. T. Butterworth, A. R. Hounsell und K. M. Prise. »Small field dosimetry for the small animal radiotherapy research platform (SARRP)«. In: *Radiation oncology (London, England)* 12.1 (2017), S. 204–204. DOI: 10.1186/s13014-017-0936-3.

[67]   A. Entezam, A. Fielding, D. Bradley und D. Fontanarosa. »Absorbed dose calculation for a realistic CT-derived mouse phantom irradiated with a standard CS-137 cell irradiator using a Monte Carlo method«. In: *PLOS ONE* 18.2 (2023). DOI: 10.1371/journal.pone.0280765.

Abbreviations

CT computed tomography.

CTV clinical target volume.

DAP$_\text{w}$ dose-area-product to water.

DDP depth dose profile.

GTV gross target volume.

HU Hounsfield unit.

IBT ion beam therapy.

IR irradiation room.

LDP lateral dose profile.

MedAustron MedAustron Ion Therapy Center.

MRI magnetic resonance imaging.

OAR organ at risk.

PC primary collimator.

PET positron emission tomography.

PTCOG Particle Therapy Co-Operative Group.

PTV planning target volume.

PV pixel value.

RBE relative radiobiological effectiveness.

RT radiation therapy.

SAD source to axis distance.

List of Abbreviations

SARRP small animal radiation research platform.

SC secondary collimator.

SCDD single crystal diamond detector.

SFDP small field dosimetry phantom.

SOBP spread-out Bragg peak.

SSD source to surface distance.

TPS treatment planning system.

WED water equivalent depth.

X-ray photon beam.